



**HAL**  
open science

## Numerical investigation of dislocation climb under stress and irradiation

Daphné da Fonseca, Fabien Onimus, Frédéric Momprou, Mihai Cosmin Marinica, Edouard de Sonis, Emmanuel Clouet, Thomas Jourdan

### ► To cite this version:

Daphné da Fonseca, Fabien Onimus, Frédéric Momprou, Mihai Cosmin Marinica, Edouard de Sonis, et al.. Numerical investigation of dislocation climb under stress and irradiation. *Acta Materialia*, 2022, 242, pp.118431. 10.1016/j.actamat.2022.118431 . cea-03884976

**HAL Id: cea-03884976**

**<https://cea.hal.science/cea-03884976v1>**

Submitted on 5 Dec 2022

**HAL** is a multi-disciplinary open access archive for the deposit and dissemination of scientific research documents, whether they are published or not. The documents may come from teaching and research institutions in France or abroad, or from public or private research centers.

L'archive ouverte pluridisciplinaire **HAL**, est destinée au dépôt et à la diffusion de documents scientifiques de niveau recherche, publiés ou non, émanant des établissements d'enseignement et de recherche français ou étrangers, des laboratoires publics ou privés.



Distributed under a Creative Commons Attribution 4.0 International License

# Numerical investigation of dislocation climb under stress and irradiation

D. Da Fonseca<sup>a,d</sup>, F. Onimus<sup>b</sup>, F. Momprou<sup>c,d</sup>, M.-C. Marinica<sup>a</sup>, E. de Sonis<sup>a</sup>,  
E. Clouet<sup>a</sup>, T. Jourdan<sup>a,\*</sup>

<sup>a</sup> *Université Paris-Saclay, CEA, Service de Recherches de Métallurgie Physique, 91191, Gif-sur-Yvette, France*

<sup>b</sup> *Université Paris-Saclay, CEA, Service de Recherches Métallurgiques Appliquées, 91191, Gif-sur-Yvette, France*

<sup>c</sup> *Centre d'Elaboration de Matériaux et d'Etudes Structurales, CNRS UPR 8011, 29 rue J. Marvig, BP 94347, Toulouse cedex 4 31055, France*

<sup>d</sup> *Université de Toulouse, UPS, F-31055 Toulouse, France*

---

## Abstract

We investigate the influence of elastic properties of point defects on dislocation climb under stress and irradiation. For this purpose, elastic dipole tensors and diaelastic polarizabilities are evaluated in aluminum for vacancies and self-interstitial atoms in their stable and saddle configurations, using density functional theory calculations. These parameters are introduced in an object kinetic Monte-Carlo code and a continuous diffusion model to estimate the stress dependence of dislocation climb, using a dipole of straight dislocations. We show that both parameters have an influence on absorption of point defects under stress, in agreement with previous analytical models. However, the effect of dipole tensor is found only 5 times larger than polarizability, whereas models predict a factor up to 30. In addition, including polarizability reverses the stress angular dependence when a uniaxial stress is applied orthogonal to the dislocation line, so in general polarizability cannot be ignored for simulations under applied stress. Further comparison with analytical models shows that they give a good description of angular dependence, provided saddle point configuration of point defects is not too anisotropic. For vacancies, which are strongly anisotropic in their saddle configuration, models fail to reproduce quantitatively lattice effects on stress angular dependence observed in simulations. Calculations show that dislocation climb velocity under irradiation is expected to be the highest if the

stress is approximately orthogonal to the dislocation line, especially along the Burgers vector, and the lowest if the stress is applied close to the  $\langle 100 \rangle$  direction with the largest projection on the dislocation line.

13 *Keywords:* Diffusion, Object kinetic Monte-Carlo, Irradiation creep,  
14 Dislocation climb, SIPA

---

## 15 **1. Introduction**

16 Under irradiation and applied stress, metallic alloys exhibit a specific deformation process known as irradiation creep [1, 2]. The associated strain rate,  
17 which may be much larger than the one associated to thermal creep, is related  
18 to anisotropic microstructural changes. Among them, anisotropic formation  
19 and growth of dislocation loops, resulting from the agglomeration of point defects (self-interstitial atoms, vacancies), have been observed [3, 4, 5, 6, 7, 8].  
20 These processes have been explained by the reorientation of small clusters under stress [9] and/or the preferred absorption of self-interstitial atoms (SIAs)  
21 and vacancies by some dislocation loops, depending on their orientation with  
22 respect to the applied stress [10]. Other mechanisms have also been proposed.  
23 They are based on climb-assisted glide of dislocations, whose anisotropic character may also come from the dependence of climb velocity on stress [11].  
24

25 Two main models have been developed to explain the preferential climb of  
26 some dislocation types under applied stress and irradiation. These two models  
27 finely depend on the elastic properties of point defects, which couple to the  
28 internal and applied strain fields and result in preferential absorption of point  
29 defects at some dislocations. They both describe a point defect through its  
30 elastic dipole, a tensor which describes how the point defect energy varies in a  
31 strain field. The first model, known as stress induced preferred absorption due  
32 to anisotropic diffusion (SIPA-AD)<sup>1</sup> [14, 15, 16, 17], relies on the anisotropy  
33 of dipole tensors of point defects in their saddle configuration [18]. Due to  
34  
35  
36

---

<sup>1</sup>In some references it is called SIPA-SAPSE (stress induced preferred absorption due to saddle-point shape effect) [12, 13]. This name has the clear advantage to identify the physical

37 this anisotropy and to the lowering of crystal symmetry by an applied stress,  
38 diffusion becomes anisotropic [19, 20]. This anisotropic diffusion is responsible  
39 for different absorption “cross-sections” by dislocations and thus for preferred  
40 absorption. The second model is the stress induced preferred absorption due  
41 to inhomogeneity interaction (SIPA-I). It is also often simply called SIPA, as  
42 it was developed first and remains very popular [21, 22, 23, 8]. It relies on the  
43 dependence of dipole tensor on local stress, a phenomenon known as diaelastic  
44 polarizability [24].

45 It is customary to quantify the effect of stress on absorption rate of defects  
46 by dislocations by calculating absorption efficiencies, which are key quantities in  
47 rate theory models. Previous analytical and numerical calculations have shown  
48 that in iron and copper, absorption efficiencies under stress exhibit a higher de-  
49 pendence on elastic dipole anisotropy than on polarizability, so that SIPA-AD  
50 could be more than one order of magnitude larger than SIPA-I [14, 12, 16]. This  
51 estimate relies on dipole tensors calculated by interatomic potentials, which can  
52 differ substantially from dipole tensors evaluated by *ab initio* methods [25]. Sev-  
53 eral approximations are made for the polarizability of the elastic dipole to make  
54 analytical calculations tractable: the four-rank tensors characterizing this polar-  
55 ization are assumed to be isotropic and identical for defects at stable and saddle  
56 positions. In addition, it is unclear what consequences approximations made in  
57 analytical models may have on the absorption rates of point defects [16]. For all  
58 these reasons, it appears important to evaluate more precisely the amplitudes  
59 of SIPA-AD and SIPA-I, *i.e.* the role of elastic dipole anisotropy and diaelastic  
60 polarizabilities on absorption efficiencies of point defects by dislocations under  
61 stress.

62 In the present work, we use two simulation methods to evaluate these ab-  
63 sorption efficiencies in aluminum. The first one is an object kinetic Monte-Carlo

---

quantum responsible for the anisotropic behavior, since anisotropic diffusion (AD) can come from various physical quantities. However, SIPA-AD seems to be more widely used in the literature, so we keep this name here.

64 (OKMC) approach, which has already been used to determine absorption effi-  
65 ciencies without applied stress [26]. The second one is a continuous diffusion  
66 model (CDM) [27]. Both methods take into account point defect properties  
67 at stable and saddle positions. To obtain a precise value of absorption effi-  
68 ciencies, dipole and polarizability tensors are extracted from density functional  
69 theory (DFT) calculations. Aluminum is chosen because it is nearly elastically  
70 isotropic, so that isotropic elasticity can be used conveniently to predict absorp-  
71 tion efficiencies [26].

72 This article is organized as follows. In section 2 diffusion of point defects  
73 under stress is discussed and the existing models of absorption efficiency under  
74 stress are shortly reviewed. Dipole tensors and diaelastic polarizabilities are cal-  
75 culated in section 3. Absorption efficiencies of point defects by dislocations are  
76 determined by OKMC and CDM and compared to existing models in section 4.

## 77 **2. Diffusion of point defects under stress and existing models of point** 78 **defect absorption efficiency**

### 79 *2.1. Diffusion under stress*

80 The migration of point defects to dislocations depends on their interaction  
81 with the elastic field created by dislocations and the applied stress. A point de-  
82 fect can be adequately described as an elastic dipole  $\Pi_{ij}$  [28, 29], which depends  
83 on the local strain field if it is polarizable (summation over repeated indexes is  
84 implied):

$$\Pi_{ij}(\boldsymbol{\varepsilon}) = P_{ij} + \alpha_{ijkl}\varepsilon_{kl}, \quad (1)$$

85 where  $P_{ij} = \Pi_{ij}(0)$  is the elastic dipole without any effect of stress,  $\alpha_{ijkl}$  the  
86 diaelastic polarizability and  $\varepsilon_{ij}$  the local strain field at the position of the point  
87 defect. The associated interaction energy can be expressed as [30]:

$$E = -P_{ij}\varepsilon_{ij} - \frac{1}{2}\varepsilon_{ij}\alpha_{ijkl}\varepsilon_{kl}. \quad (2)$$

88 Elastic dipoles and polarizabilities are in general different at stable and saddle  
89 positions. In the following, superscript “s” means that a quantity is taken at  
90 saddle position.

91 Dederichs and Schroeder have shown that the point defect flux can be written  
 92 as a function of a renormalized diffusion tensor [20]

$$\tilde{D}_{ij}(\mathbf{r}) = \frac{1}{4}D_0 \sum_{\mathbf{h}} \hat{h}_i \hat{h}_j \exp\left(-\frac{E^{s,\mathbf{h}}(\mathbf{r})}{k_{\text{B}}T}\right), \quad (3)$$

93 where  $E^{s,\mathbf{h}}(\mathbf{r})$  is the interaction energy as given by Eq. (2) for a point defect  
 94 initially located at  $\mathbf{r}$  and performing a jump  $\mathbf{h}$  with associated unit vector  $\hat{\mathbf{h}}$ ,  $D_0$   
 95 is the diffusion coefficient without stress,  $k_{\text{B}}$  the Boltzmann constant and  $T$  the  
 96 temperature. The strain field in the interaction energy is taken at the location  
 97 of the saddle point, which in the present case is  $\mathbf{r} + \mathbf{h}/2$ . The summation  
 98 is performed on all nearest neighbors. The stress free diffusion coefficient is  
 99  $D_0 = \kappa\nu_0 a^2 \exp(-E_0^{\text{m}}/k_{\text{B}}T)$ , where  $\kappa = 1$  for a vacancy and  $\kappa = 2/3$  for a  
 100  $\langle 100 \rangle$ -split dumbbell SIA. In this expression,  $a$  is the lattice parameter of the  
 101 fcc matrix,  $\nu_0$  and  $E_0^{\text{m}}$  the attempt frequency and migration energy, respectively.

102 Using a Taylor expansion to second order in strain of the diffusion coefficient,  
 103 Woo has clearly shown that different terms contribute to stress induced  
 104 preferential absorption [16]. Even though in the present work this expansion is  
 105 not used, it is useful to recall it to make the link with existing models. Let  $\varepsilon_{ij}$  be  
 106 the sum of an applied strain  $\varepsilon_{ij}^{\text{a}}$  and an internal strain  $\varepsilon_{ij}^{\text{d}}$  due to a dislocation,  
 107 which is assumed to weakly vary over distance  $a$ , so that  $\varepsilon_{ij}^{\text{d}}(\mathbf{r} + \mathbf{h}/2) \approx \varepsilon_{ij}^{\text{d}}(\mathbf{r})$ .

108 Inserting (2) into (3) leads to

$$\begin{aligned}
\tilde{D}_{ij}(\mathbf{r}) \approx & \underbrace{D_0 \delta_{ij}}_{1 - \text{stress free diffusion}} + \underbrace{\frac{1}{4} D_0 \frac{1}{k_B T} \sum_{\mathbf{h}} \hat{h}_i \hat{h}_j P_{kl}^{s, \mathbf{h}} \varepsilon_{kl}^d(\mathbf{r})}_{2 - \text{EID, first order}} \\
& + \underbrace{\frac{1}{4} D_0 \frac{1}{k_B T} \sum_{\mathbf{h}} \hat{h}_i \hat{h}_j P_{kl}^{s, \mathbf{h}} \varepsilon_{kl}^a}_{3 - \text{elastodiffusion, SIPA-AD (Woo)}} \\
& + \frac{1}{4} D_0 \frac{1}{k_B T} \sum_{\mathbf{h}} \hat{h}_i \hat{h}_j \left( \underbrace{\alpha_{klmn}^{s, \mathbf{h}}}_{4 - \text{SIPA-I}} + \underbrace{\frac{1}{k_B T} P_{kl}^{s, \mathbf{h}} P_{mn}^{s, \mathbf{h}}}_{5 - \text{SIPA-AD (Dederichs)}} \right) \varepsilon_{kl}^a \varepsilon_{mn}^d(\mathbf{r}) \\
& + \underbrace{\frac{1}{4} D_0 \frac{1}{k_B T} \sum_{\mathbf{h}} \hat{h}_i \hat{h}_j \left( \frac{1}{2} \alpha_{klmn}^{s, \mathbf{h}} + \frac{1}{2} \frac{1}{k_B T} P_{kl}^{s, \mathbf{h}} P_{mn}^{s, \mathbf{h}} \right) \varepsilon_{kl}^d(\mathbf{r}) \varepsilon_{mn}^d(\mathbf{r})}_{6 - \text{EID, second order}} \\
& + \underbrace{\frac{1}{4} D_0 \frac{1}{k_B T} \sum_{\mathbf{h}} \hat{h}_i \hat{h}_j \left( \frac{1}{2} \alpha_{klmn}^{s, \mathbf{h}} + \frac{1}{2} \frac{1}{k_B T} P_{kl}^{s, \mathbf{h}} P_{mn}^{s, \mathbf{h}} \right) \varepsilon_{kl}^a \varepsilon_{mn}^a}_{7 - \text{elastodiffusion, second order}}. \quad (4)
\end{aligned}$$

109 The first term corresponds to the diffusion tensor in the absence of stress. The  
110 second term, which is related to the elastic interaction difference (EID) for  
111 SIAs and vacancies, is responsible for the dislocation bias [31] to first order  
112 (second order is the sixth term, it is always neglected). The third term is the  
113 classical elastodiffusion term [20]. It has been identified by Woo as the main  
114 contribution to SIPA [13, 16], called SIPA-AD. The fourth and fifth terms couple  
115 the dislocation and applied strains and thus also lead to SIPA. The contribution  
116 of polarizability corresponds to SIPA-I effect [21, 22, 23], whereas the product  
117 of dipole tensors is the SIPA-AD effect as initially considered by Dederichs and  
118 Schroeder [20]. In numerical simulations based on dipole tensor anisotropy, both  
119 the third and fifth terms are included since the diffusion coefficient is kept in its  
120 initial form (3) [15]. Finally, the sixth and seventh terms are second order terms  
121 for EID and elastodiffusion. Although the latter can in principle contribute to  
122 SIPA, it has been ignored in previous studies based on polarizabilities, which  
123 all relied on analytical developments. Only the fourth term was considered.  
124 However, here again, the second part of this term is present in numerical studies

125 using anisotropic dipole tensors.

126 *2.2. Models of point defect absorption efficiency under stress*

127 In the framework of rate theory, the effect of stress on point defect absorp-  
128 tion rate by dislocations is quantified by the so-called “absorption efficiencies”.  
129 These quantities relate the absorption rate of point defects to their average con-  
130 centration in the matrix. They are obtained by solving the diffusion problem  
131 around a sink, usually at stationary state [32, 33, 34, 35, 36]. Analytical ex-  
132 pressions of absorption efficiencies can be obtained only with simple geometries  
133 and simplified description of point defect properties. Taking into account the  
134 full complexity of Eq. (4) necessarily requires numerical simulations, as those  
135 performed in the present work.

136 Heald and Speight have given an expression for the absorption efficiency of  
137 defects by dislocations under a tensile stress of magnitude  $\sigma$ , if among terms 3  
138 to 7 in Eq. (4) only the fourth one is taken into account (SIPA-I) [23]. They  
139 assume that the polarizability tensor is the same at stable and saddle points  
140 and that it is isotropic, *i.e.*

$$\alpha_{ijkl} = \left( \alpha^K - \frac{2}{3} \alpha^\mu \right) \delta_{ij} \delta_{kl} + \alpha^\mu (\delta_{ik} \delta_{jl} + \delta_{il} \delta_{jk}), \quad (5)$$

141 where  $\alpha^K$  and  $\alpha^\mu$  are the bulk and shear polarizabilities [37]. This approxima-  
142 tion amounts to considering the defect as an isotropic inhomogeneous Eshelby  
143 inclusion in the matrix. The dipole tensor is also assumed to be the same at  
144 stable and saddle points and is considered isotropic, *i.e.*  $P_{ij} = P \delta_{ij}$ . Woo has  
145 shown that the expression of Heald and Speight can be cast under the following  
146 form (HSW model) [38]:

$$Z^I(\boldsymbol{\sigma}) = Z^0 \left( 1 + \frac{\Delta Z^I(\boldsymbol{\sigma})}{Z^0} \right), \quad (6)$$



147 with

$$\frac{\Delta Z^I(\boldsymbol{\sigma})}{Z^0} = \frac{Z^0}{2\pi} \frac{\delta L(\boldsymbol{\sigma})}{L^0} \quad (7)$$

$$Z^0 = \frac{2\pi}{\ln\left(\frac{4R}{|L^0|e^\gamma}\right)} \quad (8)$$

$$L^0 = \frac{Pb}{2\pi} \frac{1-2\nu}{1-\nu} \frac{1}{k_B T} \quad (9)$$

$$\frac{\delta L(\boldsymbol{\sigma})}{L^0} = \frac{\sigma}{\mu} \left[ \frac{(1-2\nu)\alpha^K}{2(1+\nu)P} + \frac{\alpha^\mu}{3(1-2\nu)P} \left( -(1+\nu) + 3\nu(\mathbf{s} \cdot \mathbf{l})^2 + 3(\mathbf{s} \cdot \mathbf{b})^2 \right) \right] \quad (10)$$

148 (note that the  $2\pi$  factor in Eq. (7) is missing in the expression of Woo).  $Z^0$   
 149 is the absorption efficiency without applied stress. In Eqs. (8)-(10),  $\nu$  is the  
 150 Poisson's ratio,  $\mu$  is the shear modulus,  $\mathbf{b}$  is the Burgers vector ( $b = |\mathbf{b}|$ ),  $\mathbf{l}$  is  
 151 the dislocation line direction,  $\gamma$  is the Euler's constant ( $\gamma \approx 0.577$ ) and  $R$  is  
 152 the half-distance between dislocations, calculated as  $R = (\pi\rho_d)^{-1/2}$  with  $\rho_d$  the  
 153 dislocation density. The uniaxial stress is applied along  $\mathbf{s}$ , so that  $\sigma_{ij} = \sigma s_i s_j$ .  
 154 Eqs. (6) to (10) are often given with different notations, considering the defect  
 155 as an Eshelby inhomogenous inclusion. The link between the two formalisms is  
 156 recalled in Appendix A. For the sake of completeness, we note that an expression  
 157 with a similar dependence on stress orientation, in  $(\mathbf{s} \cdot \mathbf{l})^2$  and  $(\mathbf{s} \cdot \mathbf{b})^2$ , was  
 158 obtained by Wolfer and Ashkin [37].

159 With this model, the stress direction leading to the highest absorption ef-  
 160 ficiency depends on the sign of  $\alpha^\mu/P$  (Eq. (10)). For an SIA in fcc metals,  
 161 it is known that in its stable position,  $\alpha^\mu > 0$  and  $P > 0$  [39], so the model  
 162 predicts that SIAs are more absorbed by a dislocation if the tensile stress is  
 163 along the Burgers vector. For a vacancy, it is assumed in the literature that  
 164  $\alpha^\mu > 0$  [23, 22], but  $P < 0$ , so the reverse behavior is expected.

165 Later, SIPA due to elastodiffusion (SIPA-AD) was investigated analytically  
 166 by Skinner and Woo [13], Woo [16], and Borodin and Ryazanov [17]. The most  
 167 general formula was derived by Borodin and Ryazanov. They showed that if  
 168 only the three first terms in Eq. (4) are retained, and if the deviatoric part of  
 169 the dipole tensor at saddle point is small, the absorption efficiency of a defect

170 can be written as

$$Z^{\text{AD}}(\boldsymbol{\sigma}) = Z^0 \left( 1 + \frac{\Delta Z^{\text{AD},0}}{Z^0} + \frac{\Delta Z^{\text{AD,hydro}}(\boldsymbol{\sigma})}{Z^0} + \frac{\Delta Z^{\text{AD,dev}}(\boldsymbol{\sigma})}{Z^0} \right). \quad (11)$$

171 Contrary to the SIPA-I model described above, in this model, hereafter called  
 172 B&R model, the defect has different properties at stable and saddle positions.  
 173 The absorption efficiency  $Z^0$  is still defined by Eqs. (8) and (9), but  $P$  is now re-  
 174 lated to saddle point properties, *i.e.*  $P = P^{\text{s}} = \text{Tr}(\mathbf{P}^{\text{s}})/3$ .  $Z^0$  thus corresponds  
 175 to the absorption of an isotropic defect at saddle point. Saddle point anisotropy  
 176 can have an influence on absorption efficiency even in the absence of applied  
 177 stress [15, 40, 13, 17, 26, 41], this is taken into account through  $\Delta Z^{\text{AD},0}$ . The  
 178 effect of stress on absorption efficiency can be decomposed into an hydrostatic  
 179 term  $\Delta Z^{\text{AD,hydro}}$  depending only on  $\text{Tr}(\boldsymbol{\sigma})$ , and a deviatoric term  $\Delta Z^{\text{AD,dev}}$ .  
 180 Only the latter is of interest here, as we focus on the difference of absorption  
 181 efficiencies for different orientations of applied stress. For a uniaxial stress, it  
 182 reads [17, 42]

$$\frac{\Delta Z^{\text{AD,dev}}(\boldsymbol{\sigma})}{Z^0} = -\frac{\sigma}{4\mu} \frac{P^{\text{s}}}{k_{\text{B}}T} \left\{ d^{(2)} \left[ (\mathbf{s} \cdot \mathbf{l})^2 - \frac{1}{3} \right] + d^{(3)} \sum_{p=1}^3 \left[ (\mathbf{e}_p \cdot \mathbf{l})^2 (\mathbf{e}_p \cdot \mathbf{s})^2 - \frac{1}{9} \right] \right\}, \quad (12)$$

183 where  $\mathbf{e}_p$  ( $p = 1, 2, 3$ ) are the unit vectors along the crystallographic axes.  
 184 Factors  $d^{(2)}$  and  $d^{(3)}$  are related to the components of dipole tensors at saddle  
 185 point. In an fcc structure, the dipole tensor of a defect jumping along [110] is  
 186 of the form

$$\mathbf{P}^{\text{s}} = \begin{pmatrix} P_{11}^{\text{s}} & P_{12}^{\text{s}} & 0 \\ P_{12}^{\text{s}} & P_{11}^{\text{s}} & 0 \\ 0 & 0 & P_{33}^{\text{s}} \end{pmatrix}. \quad (13)$$

187 We then have  $d^{(2)} = P_{12}^{\text{s}}/P^{\text{s}}$  and  $d^{(3)} = (P_{11}^{\text{s}} - P_{33}^{\text{s}})/(2P^{\text{s}}) - P_{12}^{\text{s}}/P^{\text{s}}$ .

188 It appears from Eq. (12) that the absorption efficiency does not depend  
 189 on the orientation of uniaxial stress with respect to the Burgers vector, unlike  
 190 SIPA-I. It is generally accepted that what is important for SIPA-AD is the  
 191 orientation of stress with respect to the dislocation line direction  $\mathbf{l}$ , as shown in

192 the simplified model of Woo [16]:

$$\frac{\Delta Z^{\text{AD,dev}}(\boldsymbol{\sigma})}{Z^0} = \frac{3\sigma}{8\mu} \frac{P^{\text{s}}}{k_{\text{B}}T} \left(1 - \frac{P_1^{\text{s}}}{P^{\text{s}}}\right) \left[(\mathbf{s} \cdot \mathbf{l})^2 - \frac{1}{3}\right]. \quad (14)$$

193 This expression corresponds to Eq. (12) if  $\mathbf{l} = \mathbf{e}_p$  for a given  $p$ , except that  $P_{11}^{\text{s}}$   
 194 in Eq. (12) is replaced by the eigenvalue  $P_1^{\text{s}}$  associated to the eigenvector along  
 195 the jump direction (in practice  $P_{11}^{\text{s}}$  and  $P_1^{\text{s}}$  are very close, since  $P_1^{\text{s}} = P_{11}^{\text{s}} + P_{12}^{\text{s}}$   
 196 and  $P_{12}^{\text{s}} \ll P_{11}^{\text{s}}$ ). For vacancies,  $P^{\text{s}} < 0$  and  $P_1^{\text{s}}/P^{\text{s}} > 1$  [43, 26], so a tensile  
 197 stress applied along the dislocation line increases the absorption efficiency. For  
 198 SIAs,  $P^{\text{s}} > 0$  and  $P_1^{\text{s}}/P^{\text{s}} > 1$ , so the reverse behavior is expected. We note  
 199 however that in the general case (Eq. (12)), it is clear that the orientation of  
 200 stress with respect to crystallographic axes also plays a role.

201 Expressions for SIPA-AD and SIPA-I use only some terms in Eq. (4). In re-  
 202 ality, all terms from 3 to 7 contribute to absorption efficiency modification under  
 203 stress. As shown by Savino and Tomé [14], the third term, as a first-order term,  
 204 should give the highest contribution. However, their results were obtained with  
 205 crude estimates of polarizabilities and values of dipole tensors calculated by in-  
 206 teratomic potentials. In addition, as shown in the previous paragraphs, various  
 207 approximations underlie the analytical derivations. That is why, in the follow-  
 208 ing, we evaluate the dipole tensors and polarizabilities for both stable and saddle  
 209 configurations by DFT and introduce them into an OKMC code and a CDM  
 210 model, which take into account the full complexity of diffusion under stress.  
 211 We determine the relative importance of dipole anisotropy and polarizability by  
 212 comparing these calculations to calculations without polarizability. The validity  
 213 of expressions (7)-(10) and (12) is discussed, based on our simulation results.

### 214 **3. Point defect properties**

#### 215 *3.1. Method*

216 Point defect properties can be calculated by atomistic simulations, from the  
 217 energy difference between two simulation boxes containing a point defect, one

218 with applied homogeneous deformation  $\varepsilon$  and the other one without deforma-  
 219 tion. Following Eq. (2), it reads, for a box of volume  $V$  [44, 29],

$$\Delta E(\varepsilon) = \frac{1}{2}\varepsilon_{ij}C_{ijkl}\varepsilon_{kl}V - P_{ij}\varepsilon_{ij} - \frac{1}{2}\varepsilon_{ij}\alpha_{ijkl}\varepsilon_{kl}. \quad (15)$$

220 The first term corresponds to the homogeneous deformation of the perfect crys-  
 221 tal. It can be calculated separately with a dedicated simulation of a box without  
 222 defect and subtracted from  $\Delta E$  to retain only the contribution of the point de-  
 223 fect. By fitting Eq. (15) without bulk contribution on calculations performed  
 224 at different deformation levels, for different deformation types (shear, isotropic  
 225 dilatation, etc.), it is possible to extract point defect dipole and polarizability  
 226 tensors.

227 Another method consists in using the average residual stress on the simula-  
 228 tion box [44, 29]:

$$\sigma_{ij}(\varepsilon) = \frac{1}{V} \frac{\partial \Delta E}{\partial \varepsilon_{ij}} = C_{ijkl}\varepsilon_{kl} - \frac{1}{V} (P_{ij} + \alpha_{ijkl}\varepsilon_{kl}). \quad (16)$$

229 Elastic dipoles are readily obtained from simulations with zero applied deforma-  
 230 tion [45], after subtracting the spurious stress in the perfect simulation box [29].  
 231 Polarizabilities can be extracted from a linear fit of the stress as a function of the  
 232 deformation level, after subtraction of the contribution of the perfect crystal. If  
 233 the dipole component is also deducted, the quantity  $\Delta\sigma_{ij}(\varepsilon) = -\alpha_{ijkl}\varepsilon_{kl}/V$  is  
 234 obtained.

235 To evaluate point defect properties in aluminum, DFT calculations are per-  
 236 formed with VASP code [46, 47, 48, 49] using the projector augmented-wave  
 237 (PAW) method [50, 51]. Calculations are performed including the s states  
 238 [Ne]3s<sup>2</sup>3p<sup>1</sup>. The exchange correlation energy is evaluated using the Perdew-  
 239 Burke-Ernzerhof (PBE) generalized gradient approximation (GGA). The plane  
 240 wave energy cutoff is set to 400 eV. Brillouin zone integration is performed  
 241 with a Methfessel-Paxton broadening of 0.4 eV. Supercells with an SIA or a  
 242 vacancy contain  $256 \pm 1$  atoms. With such simulation cells, a dense shifted  
 243 Monkhorst-Pack  $k$ -point mesh grid of  $8 \times 8 \times 8$  points is necessary to obtain  
 244 converged results, in agreement with previous results [52]. Each configuration

245 is relaxed using the conjugate gradient technique. The climbing image nudged  
246 elastic band method (CI-NEB) [53] using 7 images is used in order to find saddle  
247 points. A calculation is considered as converged when the forces on each atom  
248 are lower than  $0.002 \text{ eV}/\text{\AA}$ .

249 In the present study, dipole tensors are calculated with the stress method  
250 (Eq. (16)). Simulations with interatomic potentials with different supercell sizes,  
251 reported in supplementary material, show that the error on dipole tensor compo-  
252 nents due to the interaction between the point defect and its periodic images [25]  
253 is less than 1% (Fig. S1 and Table S1). Both energy and stress methods were  
254 tested to determine polarizabilities. The convergence with the number of  $k$ -  
255 points turned out to be faster with the stress method, in agreement with previ-  
256 ous observations [54]. In addition, the stress method requires fewer deformation  
257 types to extract polarizabilities, since the different stress components are related  
258 to different combinations of  $\alpha_{ijkl}$  coefficients. For these two reasons the stress  
259 method is used. A list of the deformation types, with the corresponding values of  
260  $-V\Delta\sigma_{ij}(\boldsymbol{\varepsilon}) = \alpha_{ijkl}\varepsilon_{kl}$ , is given in Appendix B. Although the first deformation  
261 is not necessary to determine coefficients for cubic and tetragonal symmetries, it  
262 is calculated in order to check consistency of coefficients calculated by different  
263 deformations. It also gives an estimate of the error on the coefficients, which  
264 can roughly be estimated to a few eV. An additional source of error comes from  
265 the interaction of the point defect with its periodic images [62]. Simulations  
266 with interatomic potentials show that the error on polarizability tensor compo-  
267 nents with supercells of 256 atoms is less than 10 %, except one component for  
268 which it reaches 17 % (Fig. S2 and Table S1). Calculation of polarizabilities  
269 at saddle points is computationally demanding, since a NEB calculation must  
270 be performed for each deformation level of each deformation type. At least 5  
271 deformation levels are used to perform the fit.

### 272 3.2. Results

273 Dipole and polarizability tensors are given in Table 1. Dipole tensor values  
274 are slightly different from a previous DFT study [26], due to different DFT

275 settings and in particular denser  $k$ -point meshes used here. They are in good  
 276 agreement with recent DFT calculations performed on the vacancy [55]. The  
 277 relaxation volumes, deduced from the dipole tensor values through

$$\Delta V^r = \frac{\text{Tr } \mathbf{P}}{3K}, \quad (17)$$

278 where  $K = (C_{11} + 2C_{12})/3$  is the bulk modulus, are also presented in Table 1.  
 279 Altogether the values agree reasonably well with experiments, although the  
 280 absolute value of the relaxation volume of the vacancy in its stable configuration  
 281 is larger than the experimental value measured at 4 K. The tetragonal deviation  
 282 from a cubic dipole tensor for the SIA in its stable configuration is in excellent  
 283 agreement with the experimental value  $P_{11} - P_{22} = 1.1 \pm 0.3$  eV [56].

284 As can be seen from Eq. (15), introducing polarizable point defects in a  
 285 material leads to a variation of its elastic constants:

$$\Delta C_{ijkl} = -\frac{x}{\Omega} \alpha_{ijkl}, \quad (18)$$

286 where  $x$  is the atomic fraction of defects and  $\Omega$  the atomic volume. This can be  
 287 written under the more convenient form:

$$\frac{\Delta C_{ijkl}}{x C_{ijkl}} = -\frac{1}{\Omega C_{ijkl}} \alpha_{ijkl}. \quad (19)$$

288 Although  $\alpha_{ijkl}$  has a tetragonal symmetry for SIAs, it is not possible to measure  
 289 all components of the tensor experimentally. Assuming that SIA variants are  
 290 equally distributed in the material, only data related to cubic symmetry can be  
 291 extracted. Therefore it is possible to measure two shear polarizabilities

$$\alpha_{44}^* = \frac{1}{3} (\alpha_{44} + 2\alpha_{55}) \quad (20)$$

$$\alpha'^* = \frac{1}{3} \left( \frac{\alpha_{11} - \alpha_{12}}{2} + \frac{\alpha_{22} - \alpha_{12}}{2} + \frac{\alpha_{22} - \alpha_{23}}{2} \right) \quad (21)$$

292 and a bulk polarizability

$$\alpha^K = \frac{1}{3} \left( \frac{1}{3} (\alpha_{11} + 2\alpha_{12}) + \frac{2}{3} (\alpha_{22} + \alpha_{12} + \alpha_{23}) \right). \quad (22)$$

293 From Eq. (19) it is then possible to compute the influence of defects on  $C_{44}$ ,  
 294  $C' = (C_{11} - C_{12})/2$  and  $K$ . DFT results in Tab. 1 show that SIAs contribute

295 much more to the change of elastic constants than vacancies, in agreement  
296 with experimental results [57]. Vacancies make the material more compliant  
297 in compression and in shear, while SIAs are compliant in shear and stiff in  
298 compression. These variations are consistent with trends inferred from simple  
299 arguments in early works on SIPA-I [23]. The fact that SIAs are compliant in  
300 shear, which is not so intuitive, was proved with analytical models and atomistic  
301 calculations [58]. Experimental measurements also support this result. The  
302 variation in the two shear moduli,  $C_{44}$  and  $C'$ , was measured in aluminum after  
303 electron irradiation at low temperature, where only Frenkel pairs are created  
304 (Tab. 1). Negative values were obtained, in agreement with present results.  
305 We note also that  $|\Delta C_{44}/xC_{44}| > |\Delta C'/xC'|$ , which has been shown to be  
306 typical of fcc metals containing 100-dumbbells [58, 57]. Finally and perhaps  
307 most importantly, the magnitude of the change of shear moduli due to both  
308 vacancies and SIAs agrees well with experimental results. The change in bulk  
309 modulus upon introduction of point defects has not been measured in aluminum  
310 but it is expected to be small, following results obtained in Cu [59, 60]. This is  
311 confirmed by our calculations.

312 We end this section with a comment on the calculation of polarizabilities  
313 with interatomic potentials. Early calculations were made with simple pair  
314 potentials for stable [58] and saddle [30, 61] configurations. The obtained polar-  
315 izabilities were found consistent with the variation of elastic constants measured  
316 experimentally [58, 30]. However, later simulations in Cu with more physical  
317 potentials were shown to produce results at variance with experiments [62], with  
318 values of opposite signs. We encountered similar problems with potentials in  
319 aluminum, which highlights the need for DFT calculations to evaluate polariz-  
320 abilities.

Table 1: Dipole and polarizability tensors of vacancies and SIAs in their stable and saddle configurations. Entries which are not filled are zero by symmetry. Relaxation volumes and change of elastic constants due to defects, deduced from dipole tensors and polarizabilities, respectively, are compared to experimental values. Elastic constants determined by DFT are  $C_{11} = 111.4$  GPa,  $C_{12} = 60.7$  GPa and  $C_{44} = 33.1$  GPa.

	vacancy (stable)	vacancy (saddle) ([100] $\rightarrow$ [010])	SIA (stable) ([100])	SIA (saddle) ([100] $\rightarrow$ [010])
$P_{11}$ (eV)	-2.49	-2.15	18.71	18.57
$P_{22}$ (eV)	$= P_{11}$	$= P_{11}$	17.80	$= P_{11}$
$P_{33}$ (eV)	$= P_{11}$	1.96	$= P_{22}$	18.40
$P_{12}$ (eV)		-0.22		1.45
$\alpha_{11}$ (eV)	23	41	-10	4
$\alpha_{33}$ (eV)	$= \alpha_{11}$	-3	-13	-8
$\alpha_{44}$ (eV)	4	7	103	73
$\alpha_{55}$ (eV)	$= \alpha_{44}$	$= \alpha_{44}$	41	$= \alpha_{44}$
$\alpha_{66}$ (eV)	$= \alpha_{44}$	15	$= \alpha_{55}$	62
$\alpha_{36}$ (eV)		9		0
$\alpha_{16}$ (eV)		-1		-12
$\alpha_{45}$ (eV)		10		25
$\alpha_{23}$ (eV)	$= \alpha_{12}$	$= \alpha_{13}$	-45	$= \alpha_{13}$
$\alpha_{13}$ (eV)	$= \alpha_{12}$	2	$= \alpha_{12}$	-56
$\alpha_{12}$ (eV)	13	19	-60	-71
$\Delta V^r/\Omega$ (sim.)	-0.31	-0.10	2.27	
$\Delta V^r/\Omega$ (exp.)	$-0.05 \pm 0.05^{(a)}$ $-0.36^{(b)}$	$-0.19^{(d)}$	$1.9 \pm 0.2^{(a,c)}$	
$\frac{\Delta C_{44}}{xC_{44}}$ (sim.)	-1.2		-18.1	
$\frac{\Delta C_{44}}{xC_{44}}$ (exp.) <sup>(e)</sup>			$-23 \pm 2$	
$\frac{\Delta C'}{\Delta C'}$ (sim.)	-1.9		-8.2	
$\frac{\Delta C'}{\Delta C'}$ (exp.) <sup>(e)</sup>			$-13 \pm 2$	
$\frac{\Delta K}{xK}$ (sim.)	-2		5	

<sup>(a)</sup> Measurement at 4 K, Reference [63].

<sup>(b)</sup> Measurement at 700 K, Reference [64].

<sup>(c)</sup> Reference [65].

<sup>(d)</sup> Reference [66], using formation volume of Ref. [64].

<sup>(e)</sup> After subtraction of the anharmonic effect due to volume expansion [57]. This value corresponds to the sum of SIA and vacancy contributions, but it is often considered that vacancy contribution is small [39, 57], which is confirmed by measurements on quenched samples [67].



321 **4. Effect of stress orientation on point defect absorption by disloca-**  
322 **tions**

323 *4.1. Methods*

324 In this part, we evaluate the absorption efficiencies of point defects by dis-  
325 locations in the configuration shown in Fig. 1. The system contains two dis-  
326 locations of opposite Burgers vectors  $\mathbf{b} = \pm a/2[10\bar{1}]$  and line direction  $\mathbf{l} =$   
327  $1/\sqrt{6}[\bar{1}2\bar{1}]$ . The vector normal to the glide plane is  $\mathbf{n} = 1/\sqrt{3}[111]$ . The lattice  
328 is rotated to align the dislocations along the direction  $\mathbf{u}_z$  of the orthorhombic  
329 box and the Burgers vectors along  $\mathbf{u}_x$ . The dimension of the system is  $d$  along  
330  $y$  and  $2d$  along  $x$ , with  $d = 100$  nm, and the dislocations are located at  $d/2$  and  
331  $3d/2$  along  $x$ . This corresponds to a dislocation density  $\rho_d = 10^{14} \text{ m}^{-2}$ , which  
332 is typical of steady state dislocation densities of irradiated microstructures [68].  
333 Along  $z$ , the system consists of a thin slab of 1 nm. Periodic boundary condi-  
334 tions are used in the three directions. This arrangement of dislocations was used  
335 in a previous study [26], it ensures a proper convergence of the strain field when  
336 the contribution of dislocations in periodic replica is taken into account [69], if  
337 the strain field is evaluated with isotropic elasticity. It has been checked pre-  
338 viously that in aluminum, using isotropic elasticity has a negligible effect on  
339 absorption efficiencies [26], so we use this approximation here. This also per-  
340 mits to increase the computational efficiency of OKMC simulations. The shear  
341 modulus is  $\mu = 26$  GPa and the Poisson's ratio is  $\nu = 0.35$  [26]. Other disloca-  
342 tion arrangements could have been chosen; with such dislocation densities they  
343 would give slightly different values of absorption efficiencies [35]. However, the  
344 dependence of absorption efficiencies on stress orientation is expected to be the  
345 same.

346 To determine absorption efficiencies, vacancies and SIAs are considered sep-  
347 arately. Point defects are uniformly generated in the system and they are ab-  
348 sorbed if they reach one of the cylinders of radius  $r_c = 2b$  centered on disloca-  
349 tions. The mean field equation describing the evolution of point defect average

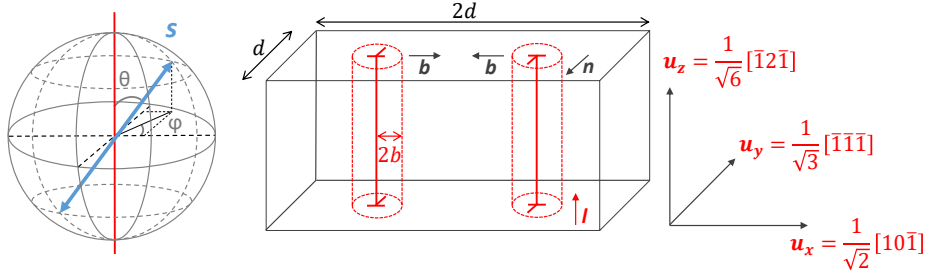


Figure 1: System simulated containing a dipole of straight dislocations. A tensile stress  $\sigma$  is applied along  $\mathbf{s}$ , given by the two angles  $(\theta, \varphi)$ .

350 concentration  $\bar{C}$  is

$$\frac{d\bar{C}}{dt} = G - Z\rho_d D_0 \bar{C}, \quad (23)$$

351 where  $G$  is the creation rate. The absorption efficiency is deduced at steady  
352 state from the measurement of  $\bar{C}$ :

$$Z = \frac{G}{\rho_d D_0 \bar{C}}. \quad (24)$$

353 A convenient method to determine  $\bar{C}$  is object kinetic Monte-Carlo [26].  
354 Point defects are introduced at a constant rate in the simulation box. They  
355 perform atomic jumps until they are absorbed by one of the dislocations. For  
356 a point defect located at  $\mathbf{r}$ , jump frequencies are calculated for each jump  $\mathbf{h}$ ,  
357 using the following expression:

$$\Gamma^{\mathbf{h}}(\mathbf{r}) = \nu_0 \exp\left(-\frac{E_0^m + E^s(\mathbf{r} + \mathbf{h}/2) - E^e(\mathbf{r})}{k_B T}\right), \quad (25)$$

358 where, as in section 2,  $\nu_0$  and  $E_0^m$  are the attempt frequency and the migra-  
359 tion energy without elastic interactions,  $E^e$  and  $E^s$  are the interaction energies  
360 with the local strain field at stable and saddle points, respectively (Eq. (2)).  
361 Events (defect jumps and creation of point defects) are chosen following the  
362 residence time algorithm [70, 71]. Transition of SIAs to  $\langle 110 \rangle$  crowdion config-  
363 uration, highlighted recently in copper under high local shear strain [72], is not  
364 considered. More details on OKMC simulations can be found in Ref. [26].

365 For a given creation rate, it is possible to determine  $Z$  by calculating the  
366 average number of point defects in the simulation box at steady state (Eq. (24)).

367 The physical time of the simulations is chosen to ensure the convergence of  $Z$ . To  
 368 provide a confidence interval, the standard deviation is computed with a block-  
 369 averaging procedure [73]. On all graphs, the error bars in figures correspond to  
 370 the standard deviation.

371 An alternative to OKMC is the continuous diffusion model (CDM), as de-  
 372 scribed in Ref. [27]. This approach has been shown to produce results in close  
 373 agreement with reference OKMC simulations; in particular, it can properly  
 374 handle the interaction of point defects with sinks in their stable and saddle po-  
 375 sitions, as explicitly done in OKMC. The equation to be solved is based on the  
 376 expression of the renormalized diffusion tensor given in Eq. (3):

$$G - \nabla \cdot \mathbf{J} = 0, \quad (26)$$

377 with

$$\mathbf{J}(\mathbf{r}) = -\tilde{\mathbf{D}}(\mathbf{r})\nabla u(\mathbf{r}). \quad (27)$$

378 In this equation,  $u$  is a renormalized concentration, which accounts for the  
 379 concentrations of the different configurations of defects in their stable position  
 380 (for SIAs) [20, 27]. Contrary to OKMC, CDM is a local approach, *i.e.* it  
 381 amounts to taking  $E^s$  in Eq. (25) at  $\mathbf{r}$  instead of  $\mathbf{r} + \mathbf{h}/2$ . In practice, for  
 382 weakly varying elastic fields, this approximation is valid. CDM calculations are  
 383 similar to phase field calculations in this context [41].

384 Since it is deterministic in nature, CDM produces results which are free  
 385 of statistical error. However, the finite element solving of the continuity equa-  
 386 tion (26) may be quite CPU and memory demanding for large three-dimensional  
 387 systems, as fine meshing is required near the sink where concentrations and elas-  
 388 tic fields vary steeply. Therefore, this method is especially useful for systems  
 389 which are invariant along at least one direction. This is the case of the con-  
 390 figuration shown in Fig. 1, which is invariant along  $z$ . Although absorption  
 391 efficiencies can be obtained with a two-dimensional system, we use a thin slab  
 392 of 1 nm along  $z$  and impose periodic boundary conditions, as in OKMC.

393 In the following, simulations are performed at  $T = 300$  K. A uniaxial tensile  
 394 stress of 100 MPa is applied along  $(\theta, \varphi)$  (Fig. 1). Although this value is rather

395 high for aluminum (the yield stress of very large grained pure aluminum is  
 396 around 10 MPa), it permits to obtain a better convergence with OKMC. We  
 397 have checked, by varying the stress amplitude, that at such levels of stress the  
 398 absorption efficiency is linear in  $\sigma$ . So the results can easily be extrapolated to  
 399 lower values of stress. The effect of elastodiffusion is investigated with OKMC,  
 400 which is our reference method. We check that in this case, CDM produces  
 401 results in agreement with OKMC. To determine the effect of polarizability, we  
 402 subtract the absorption efficiencies obtained with and without polarizability.  
 403 As we need very high accuracy on the absorption efficiencies to perform the  
 404 subtraction, CDM is used in this case.

## 405 *4.2. Results*

### 406 *4.2.1. SIPA-AD*

407 As explained above, for SIPA-AD the interaction energy of point defects is  
 408 based solely on elastic dipoles. To evaluate this first mechanism, we start with  
 409 OKMC simulations. A 3D map representing the influence of tensile stress ori-  
 410 entation on absorption efficiency is shown in Fig. 2. We represent the difference  
 411 of absorption efficiencies for a uniaxial stress of magnitude  $\sigma$  and a hydrostatic  
 412 stress with the same value of  $\text{Tr}(\boldsymbol{\sigma})$ , called  $\Delta Z_1^{\text{AD}}$  for SIAs and  $\Delta Z_v^{\text{AD}}$  for va-  
 413 cancies. This quantity corresponds to  $\Delta Z^{\text{AD,dev}}$  in the decomposition shown in  
 414 Eq. (11). From Fig. 2 we see that vacancy absorption is increased if the stress  
 415 is applied close to a direction ( $\theta = 30^\circ, \varphi = 90^\circ$ ). Directions that favor SIA  
 416 absorption are more or less spread on a strip tilted with respect to the plane  
 417 orthogonal to the line direction.

418 To provide a more quantitative representation and facilitate the comparison  
 419 with CDM and B&R model (Eq. (12)),  $\Delta Z^{\text{AD}}$  is plotted in Figs. 3 and 4 as a  
 420 function of  $\theta$ , for  $\varphi = 0^\circ$  (in the slip plane  $(\mathbf{l}, \mathbf{b})$ ) and  $\varphi = 90^\circ$  (in the climb  
 421 plane  $(\mathbf{l}, \mathbf{n})$ ). Results obtained with CDM are in very good agreement with  
 422 OKMC, which validates CDM to calculate sink strengths in this configuration.  
 423 B&R model is able to qualitatively reproduce the effect of stress on absorption  
 424 efficiency. In particular, the dependence on  $\varphi$  is correctly taken into account,

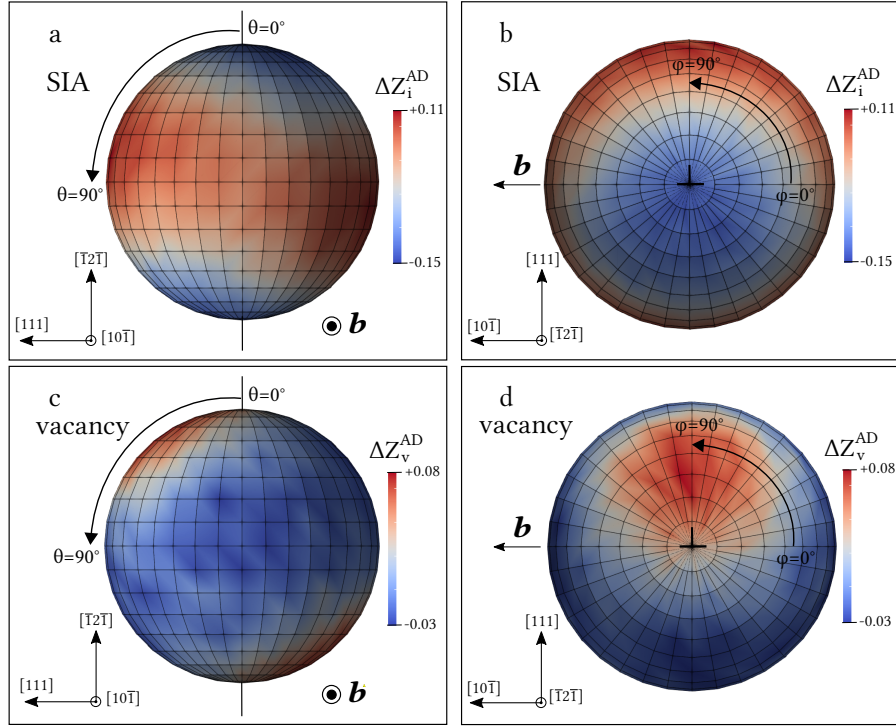


Figure 2: Difference of absorption efficiency  $\Delta Z^{\text{AD}}$  (see text for the definition) of a straight dislocation dipole in relation to the tensile stress orientation, represented on a unit sphere by a color scale for SIA-AD mechanism when only  $P_{ij}$  is accounted for in the interaction energy. A tensile stress of 100 MPa is applied, scanning space with a  $10^\circ$  step. The dislocation is along  $[\bar{1}2\bar{1}]$  and the Burgers vector is along  $\pm[10\bar{1}]$ . The SIA results are presented in (a) and (b) and the vacancy results in (c) and (d). For the sake of clarity only one dislocation is schematically represented.

425 unlike the model of Woo which only depends on  $\theta$  (not shown). However,  
 426 the amplitude of  $\Delta Z^{\text{AD}}$  is underestimated with B&R model, especially for the  
 427 vacancy with a factor up to 3 at  $\theta = 30^\circ$  and  $\varphi = 90^\circ$ , where the absorption  
 428 efficiency is maximum.

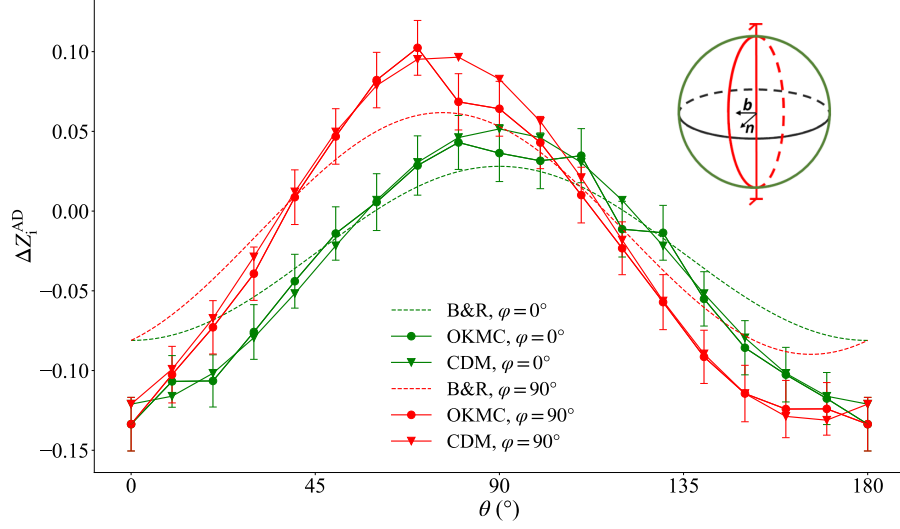


Figure 3: Difference of absorption efficiency  $\Delta Z^{\text{AD}}$  (see text for the definition) of a straight dislocation dipole for SIAs as a function of  $\theta$  (angle between tensile stress and dislocation line  $\mathbf{l}$ ) for SIPA-AD mechanism, with only  $P_{ij}$  accounted for in the interaction energy. Results obtained by OKMC and CDM are compared. The analytical B&R model of Eq. (12) is shown in dashed lines. The absorption efficiency is presented for two values of  $\varphi$ :  $\varphi = 0^\circ$ , *i.e.* in a plane containing  $\mathbf{l}$  and  $\mathbf{b}$  and  $\varphi = 90^\circ$ , *i.e.* in a plane containing  $\mathbf{l}$  and  $\mathbf{n}$ .

#### 429 4.2.2. SIPA-I

430 To determine the effect of polarizability, absorption efficiencies obtained with  
 431 dipole tensors only are subtracted from those obtained with both dipole and  
 432 polarizability tensors taken into account. These quantities are noted  $\Delta Z^{\text{I}}$ . As  
 433 discussed above, CDM is used for the two calculations to obtain results free  
 434 from statistical errors.

435 Absorption efficiencies of SIAs and vacancies are the highest along two dif-  
 436 ferent specific directions of applied stress (Fig. 5). Absorption of SIAs is more

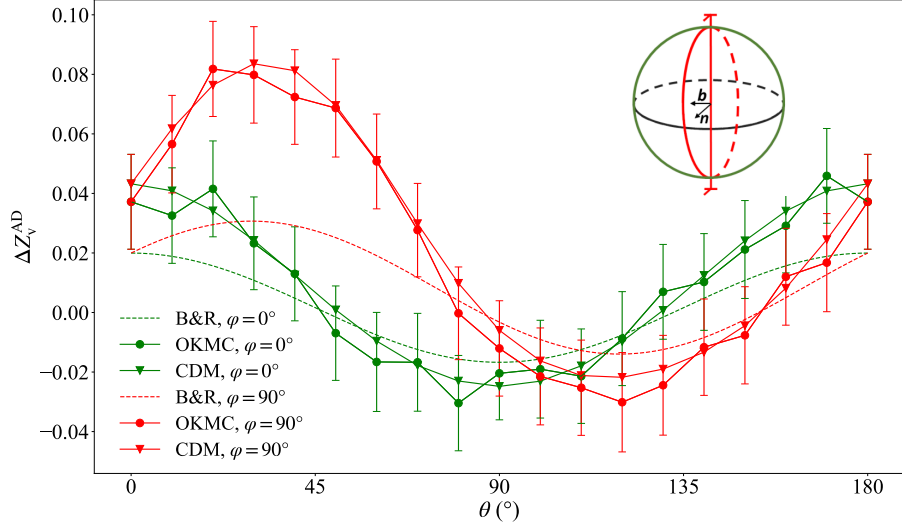


Figure 4: Difference of absorption efficiency  $\Delta Z_v^{\text{AD}}$  (see text for the definition) of a straight dislocation dipole for vacancies as a function of  $\theta$  (angle between tensile stress and dislocation line  $l$ ) for SIPA-AD mechanism, with only  $P_{ij}$  accounted for in the interaction energy. Results obtained by OKMC and CDM are compared. The analytical B&R model of Eq. (12) is shown in dashed lines. The absorption efficiency is presented for two values of  $\varphi$ :  $\varphi = 0^\circ$ , *i.e.* in a plane containing  $l$  and  $b$  and  $\varphi = 90^\circ$ , *i.e.* in a plane containing  $l$  and  $n$ .

437 efficient if the stress is applied along the Burgers vector, in agreement with  
 438 early estimates of SIPA-I [21, 23, 38]. The influence of polarizability on va-  
 439 cancy absorption under stress is more surprising. It appears quite similar to  
 440 the effect of dipole tensor anisotropy, with a direction of preferential absorption  
 441 along ( $\theta = 30^\circ$ ,  $\varphi = 90^\circ$ ). With the existing SIPA-I model, one expects a low  
 442 absorption rate if the stress is applied along the Burgers vector and a higher  
 443 absorption rate for other stress orientations.

444 To provide a more quantitative comparison with HSW model (Eqs. (7)-(10)),  
 445 which assumes that point defects have the same isotropic properties at stable  
 446 and saddle positions, the values of dipole tensor  $P$  and polarizabilities  $\alpha^\mu$  and  
 447  $\alpha^K$  are deduced from properties of defects in Tab. 1 taken at stable position.  $P$ ,  
 448 calculated as  $\text{Tr}(\mathbf{P})/3$ , is equal to 18.10 eV for SIAs and  $-2.49$  eV for vacancies.

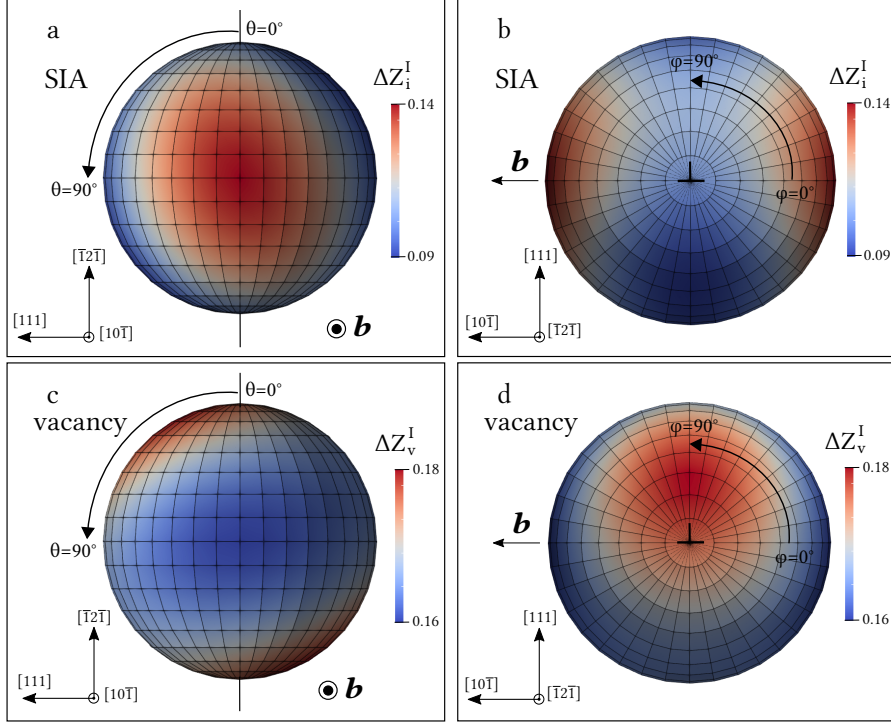


Figure 5: Absorption efficiency increment  $\Delta Z^I$  of point defects by a straight dislocation dipole in relation to the tensile stress orientation, represented on a unit sphere by a color scale, due to polarizability  $\alpha_{ijkl}$  (SIPA-I). Values are obtained by CDM. They result from the difference between absorption efficiencies with  $P_{ij}$  and  $\alpha_{ijkl}$  considered and with only  $P_{ij}$  included. A tensile stress of 100 MPa is applied, scanning space with a  $10^\circ$  step. The dislocation is along  $[\bar{1}\bar{2}\bar{1}]$  and the Burgers vector is along  $\pm[10\bar{1}]$ . The SIA results are presented in (a) and (b) and the vacancy results in (c) and (d).



449 Shear polarizability can be expressed as a Voigt average

$$\alpha^\mu = \frac{3}{5}\alpha_{44}^* + \frac{2}{5}\alpha'^*, \quad (28)$$

450 where  $\alpha_{44}^*$  and  $\alpha'^*$  are given by Eqs. (20) and (21) respectively. We have  
 451  $\alpha^\mu = 45.6$  eV for SIAs and  $\alpha^\mu = 4.4$  eV for vacancies. Bulk polarizability,  
 452 as calculated with Eq. (22), is  $\alpha^K = -40.7$  eV for SIAs and  $\alpha^K = 16.3$  eV for  
 453 vacancies.

454 The effect of SIPA-I is usually discussed for a tensile stress orthogonal to the  
 455 dislocation line ( $\theta = 90^\circ$ ), either along the Burgers vector ( $\varphi = 0^\circ$ ) or orthogonal  
 456 to it ( $\varphi = 90^\circ$ ) [23]. The variation of absorption efficiency with  $\varphi$ , with  $\theta = 90^\circ$ ,  
 457 is shown in Figs. 6 and 7 for SIAs and vacancies, respectively. Some terms are  
 458 dropped in Eq. (6), which may explain why results are shifted with respect to  
 459 CDM. This shift is not relevant to our purpose. Leaving this aspect aside, the  
 460 agreement between CDM results and HSW model for  $\theta = 90^\circ$  is remarkable  
 461 for the two defects. Results for  $\theta = 30^\circ$ , including the direction where  $\Delta Z_v^I$  is  
 462 maximum, are also reported in these figures. The analytical solution departs  
 463 appreciably from CDM, especially for the vacancy. The amplitude of SIPA-I for  
 464 the vacancy is lower than the result from CDM by more than a factor two.

### 465 4.3. Discussion

#### 466 4.3.1. SIPA-AD

467 The contribution of intrinsic dipole anisotropy at saddle configuration to  
 468 SIPA (SIPA-AD) has been discussed by several authors [19, 20, 15, 13, 16, 17].  
 469 It was shown that the absorption efficiency is mostly dependent on the direction  
 470 of uniaxial stress with respect to the dislocation line [15, 13]. Under stress,  
 471 the diffusion tensor becomes anisotropic, owing to saddle point anisotropy. A  
 472 dislocation orthogonal to the direction of fastest diffusion will capture more  
 473 point defects than a dislocation collinear to it, because its “cross section” for  
 474 defect absorption is higher (the term “cross-section” is only strictly valid for  
 475 purely 1D diffusion, *i.e.* for an infinitely large effect of stress). Directions of  
 476 fast diffusion depend on the values of dipole tensor at saddle configuration.

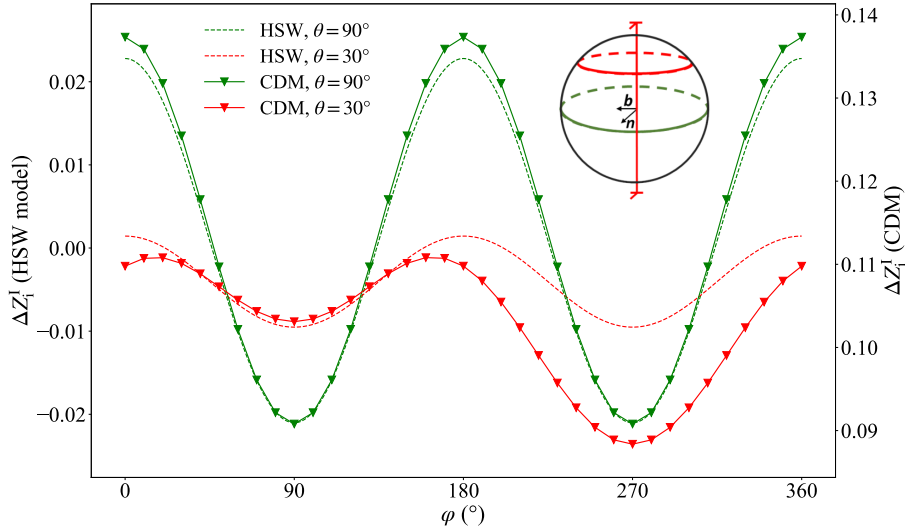


Figure 6: Increment of absorption efficiency  $\Delta Z_i^I$  due to polarizability of SIAs, as a function of  $\varphi$ , for two values of  $\theta$  ( $30^\circ$  and  $90^\circ$ ). Results are obtained with CDM and compared to HSW model given by Eqs. (7)-(10).

477 Vacancies diffuse preferentially in a plane orthogonal to the applied stress [74],  
 478 which explains why vacancy absorption is enhanced when the tensile direction  
 479 is collinear to the dislocation line. The behavior of SIAs is explained with the  
 480 same reasoning [16].

481 We have seen in Fig. 2 that our simulations and B&R model are in quali-  
 482 tative agreement with these conclusions. However, the direction of maximum  
 483 absorption of vacancies is shifted by about  $30^\circ$  with respect to the line direc-  
 484 tion in the plane defined by  $(\mathbf{l}, \mathbf{n})$  ( $\varphi = 90^\circ$ ). Likewise, the strip of maximum  
 485 absorption for SIAs is tilted, with a maximum at around  $\theta = 70^\circ$  in the plane  
 486  $(\mathbf{l}, \mathbf{n})$  and  $\theta = 90^\circ$  in the plane  $(\mathbf{l}, \mathbf{b})$  ( $\varphi = 0^\circ$ ). These discrepancies can be ex-  
 487 plained by lattice effects, which are not all taken into account in Woo's approach  
 488 (Eq. (14)), unlike B&R model (Eq. (12)).

489 To explain these results, we consider a uniaxial stress  $\sigma_{ij} = \sigma s_i s_j$ , with  
 490  $s_1 = \sin \alpha \cos \beta$ ,  $s_2 = \sin \alpha \sin \beta$ ,  $s_3 = \cos \beta$  the three direction cosines of  $\mathbf{s}$  in

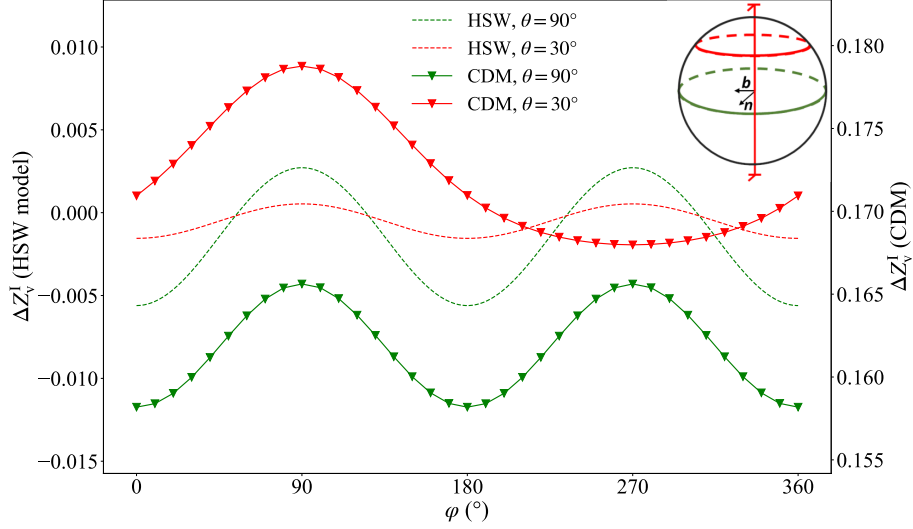


Figure 7: Increment of absorption efficiency  $\Delta Z_v^I$  due to polarizability of vacancies, as a function of  $\varphi$ , for two values of  $\theta$  ( $30^\circ$  and  $90^\circ$ ). Results are obtained with CDM and compared to HSW model given by Eqs. (7)-(10).

491 the basis  $([100], [010], [001])$ . We have

$$\varepsilon_{ij} = \frac{\sigma}{E} (s_i s_j (1 + \nu) - \nu \delta_{ij}), \quad (29)$$

492 with  $E = 2\mu(1 + \nu)$  Young's modulus. We consider a jump along  $[110]$ , for  
 493 which the dipole tensor at saddle position is given by Eq. (13). Neglecting the  
 494 polarizability, the saddle point energy reads

$$E^s = -\frac{\sigma}{E} (P_{11}(1 + \nu) \sin^2 \alpha - 2\nu P_{11} + P_{33}(1 + \nu) \cos^2 \alpha - \nu P_{33} \\ + P_{12}(1 + \nu) \sin^2 \alpha \sin 2\beta). \quad (30)$$

495 Given the signs of the dipole tensor components of a vacancy (see Tab. 1),  
 496 it is clear that the energy is minimum for  $\alpha = 0^\circ$ , *i.e.* for a stress applied along  
 497  $[001]$ . For the SIA, since  $P_{12} > 0$ , we must have  $\beta = 45^\circ$ . In addition, with  
 498  $P_{11} + P_{12} > P_{33}$  the energy is minimum for  $\alpha = 90^\circ$ . This means the stress  
 499 must be applied along the jump direction to minimize the saddle point energy.

500 As already discussed, to obtain the maximum absorption efficiency by a  
 501 dislocation, one must favor the jumps which are as orthogonal as possible to

502 this dislocation. For a dislocation along  $\mathbf{l} = [\bar{1}2\bar{1}]/\sqrt{6}$ , there are two jumps  
 503 which are orthogonal to the dislocation line, highlighted in red in Fig. 8-(a).  
 504 These jumps are favored if the stress is applied along  $[010]$ . This configuration  
 505 corresponds to  $\theta = 35^\circ$ , in close agreement with our OKMC and CDM results  
 506 ( $\theta \approx 33^\circ$ ) and B&R results ( $\theta = 29^\circ$ ). The absorption rate of SIAs should be  
 507 large if the stress is applied along the direction of the two jumps orthogonal to  
 508 the line direction, represented in green in Fig. 8-(b). The jump direction is along  
 509  $\mathbf{b}$ , and it can be seen in Fig. 2 that indeed, this direction is located in the strip  
 510 of high absorption rates. It is actually the direction of highest absorption rate  
 511 in the plane  $(\mathbf{l}, \mathbf{b})$  ( $\varphi = 0^\circ$ ). From Fig. 2 it appears that maximum absorption  
 512 rates are obtained in a plane  $(\mathbf{l}, \mathbf{n})$  ( $\varphi = 90^\circ$ ). For a stress applied in this plane,  
 513 the projection of  $\mathbf{s}$  on the jumps represented in red in Fig. 8-(b) is the highest  
 514 for  $\theta = 71^\circ$ ; these four jumps are not orthogonal to the dislocation, but their  
 515 projection on  $\mathbf{l}$  is small. The fact that four jumps contribute to SIA diffusion  
 516 enhancement in this case explains why the absorption rate is even higher than  
 517 for  $\mathbf{s}$  along  $\mathbf{b}$ . The value of  $\theta$  found is very close to OKMC and CDM results  
 518 ( $\theta = 76^\circ$ , Fig. 3) and B&R results ( $\theta = 76^\circ$ ). The variation of  $\theta$  from  $90^\circ$   
 519 to  $71^\circ$  as  $\varphi$  varies from  $0^\circ$  to  $90^\circ$  explains the tilted strip in Fig. 2. Finally,  
 520 we note that in this discussion, the strain field of the dislocation has not been  
 521 considered. This validates the assumption of Woo to neglect the dislocation  
 522 field in the analytical treatment [16]. Fully considering lattice effects as in B&R  
 523 model appears necessary to obtain a good agreement with OKMC and CDM. We  
 524 note that although second order terms in Eq. (4) (fifth term and second part of  
 525 seventh term) can in principle also contribute to SIPA-AD, they certainly have  
 526 a very small impact as they are included in OKMC and CDM but not in B&R  
 527 model.

528 Even though B&R model successfully reproduces lattice effects, the magni-  
 529 tude of  $\Delta Z^{\text{AD}}$  is significantly different from our calculations for both defects.  
 530 This is especially the case for the vacancy. In the direction of applied stress  
 531 where the absorption efficiency is the highest, the discrepancy reaches a fac-  
 532 tor of around 3. For this direction, the effects of anisotropy of dipole tensor

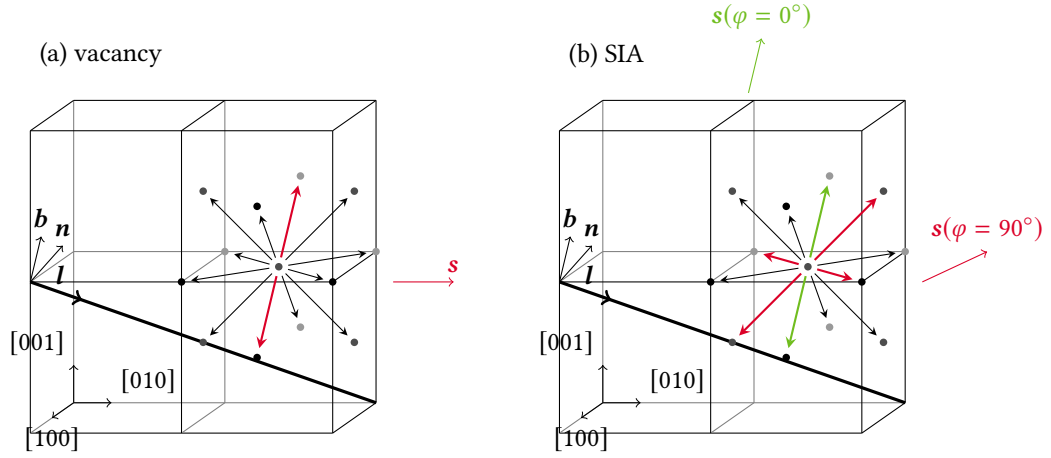


Figure 8: Orientation of uniaxial stress  $\mathbf{s}$  leading to maximum absorption of point defects by a dislocation of line direction  $\mathbf{l} = [\bar{1}2\bar{1}]/\sqrt{6}$  and Burgers vector  $\mathbf{b} = [\bar{1}01]/\sqrt{2}$  ( $\mathbf{n} = [111]/\sqrt{3}$ ), and associated jumps responsible for this high absorption rate. (a) Absorption of vacancies (b) Absorption of SIAs; here we give the orientation of stress if it is applied in the planes defined by  $(\mathbf{l}, \mathbf{b})$  ( $\varphi = 0^\circ$ ) and  $(\mathbf{l}, \mathbf{n})$  ( $\varphi = 90^\circ$ ). The maximum absorption rate is obtained in this latest case, with four jumps contributing significantly to the absorption of SIAs.

533 at saddle configuration are the highest. In the model developed by Borodin  
 534 and Ryazanov, the deviatoric part of the dipole tensor is assumed to be small  
 535 compared to the hydrostatic part. This is not true for the vacancy, so it is not  
 536 surprising that the model cannot quantitatively reproduce the values of  $\Delta Z^{\text{AD}}$   
 537 when the dipole anisotropy contributes significantly to the absorption efficiency.

#### 538 4.3.2. SIPA-I

539 Contrary to SIPA-AD, the dislocation strain field is an essential ingredient  
 540 in SIPA-I. The fourth term in Eq. (4), which induces a coupling between the  
 541 applied field and the dislocation field, gives rise to preferential diffusion of point  
 542 defects to some dislocations. Usually, one considers that SIAs are the main  
 543 contributors to SIPA-I, due to their large polarizability [75, 76, 38, 14, 77].  
 544 HSW model (Eqs. (7)-(10)) predicts that SIAs will be absorbed preferentially by  
 545 dislocations whose Burgers vector is aligned with the applied stress [22, 23, 38].

546 Our DFT calculations confirm that SIAs are much more polarizable than

547 vacancies (Tab. 1). Shear polarizabilities of SIAs and vacancies at stable point,  
 548 which are used in the analytical model, are found to differ by around one order  
 549 of magnitude. However, the effect of vacancies on SIPA-I is not completely neg-  
 550 ligible (Fig. 5): the amplitude of the effect is only three times smaller than for  
 551 SIAs. This is essentially due to the high absorption efficiency of vacancies when  
 552 the stress is applied in the plane  $(\mathbf{l}, \mathbf{n})$ , for  $\theta = 25^\circ$ , close to the direction corre-  
 553 sponding to a maximum of absorption efficiency for SIPA-AD ( $\theta = 33^\circ$ ). This  
 554 behavior is not captured by HSW model. Additional calculations (not shown)  
 555 performed with CDM and using isotropic and identical properties at stable and  
 556 saddle points led to results in close agreement with HSW model. We can con-  
 557 clude that this model is accurate in its framework and that the discrepancy  
 558 observed here is certainly due to lattice effects. On the contrary, the agreement  
 559 between the model and CDM is rather satisfactory for SIAs, although some  
 560 discrepancies appear if the stress is not normal to the dislocation line. This  
 561 shows that in general, since polarizabilities induce second order contributions,  
 562 they should not be considered without taking into account the first order con-  
 563 tributions, *i.e.* of dipole anisotropy. To our knowledge, our simulations are  
 564 the first estimations of SIPA-I based on full account of first order terms and  
 565 polarizabilities at saddle configurations.

566 As for SIPA-AD, other terms potentially contributing to SIPA are included  
 567 in CDM but not in the model. The first part of the seventh term in Eq. (4)  
 568 leads to anisotropic diffusion, so to SIPA. However, for applied strains of the  
 569 order of  $10^{-4}$  as those considered here, this term can be safely neglected.

#### 570 *4.3.3. Relative contributions of SIPA-AD and SIPA-I to dislocation climb under* 571 *stress*

572 From analytical expressions as (6) and (11), it has been suggested that SIPA-  
 573 AD is up to thirty times larger than SIPA-I [14, 12, 16]. It is interesting to see  
 574 whether the present calculations, with more accurate values of dipole tensors  
 575 and polarizabilities, confirm this conclusion. Indeed, considering polarizabilities  
 576 induces additional complexity in kinetic codes, so it is useful to assess the rel-

577 evance of including them. From Figs. 2 and 5, one sees that the amplitude of  
578 absorption efficiencies considering intrinsic dipole anisotropy only (SIPA-AD) is  
579 around five times larger than the one due to polarizability (SIPA-I), whatever  
580 the defect. However, as shown in Fig. 9, for a stress applied in a plane normal  
581 to the dislocation line, polarizability reverses the directions of favored absorp-  
582 tion of SIAs. The reason for this is the low effect of dipole anisotropy in this  
583 plane, at variance with polarizability. This suggests that polarizabilities cannot  
584 be disregarded for studies under stress.

585 Including intrinsic dipole anisotropy and polarizability in the calculations  
586 permits to conclude about the directions of applied stress which favor SIA or  
587 vacancy absorption. From the present results it can be concluded that if the  
588 stress is approximately orthogonal to the dislocation line, and in particular along  
589 the Burgers vector, the net absorption rate of SIAs should be the highest. On  
590 the contrary, a uniaxial stress applied close the  $\langle 100 \rangle$  direction with the largest  
591 projection on the dislocation line should minimize the net absorption rate of  
592 SIAs. Since climb velocity under irradiation is generally driven by an excess of  
593 absorbed SIAs due to EID, the climb velocity is expected to increase in the first  
594 configuration and to decrease in the second one.

## 595 **5. Conclusion**

596 In this study we have investigated the effect of an applied uniaxial stress on  
597 point defect absorption by straight dislocations in aluminum. Elastic dipoles and  
598 diaelastic polarizabilities of vacancies and SIAs have been calculated by DFT at  
599 stable and saddle points. These parameters have been used in an OKMC code  
600 and a CDM model to evaluate absorption efficiencies under stress. Our results  
601 confirm that the amplitude of SIPA-I, due to polarizability, is lower than the  
602 one of SIPA-AD, due to dipole anisotropy, by a factor of around five. However,  
603 the correct behavior of the absorption efficiency in a plane orthogonal to the  
604 dislocation line can only be obtained if polarizability is considered, so neglecting  
605 polarizability in studies under stress may not be appropriate.

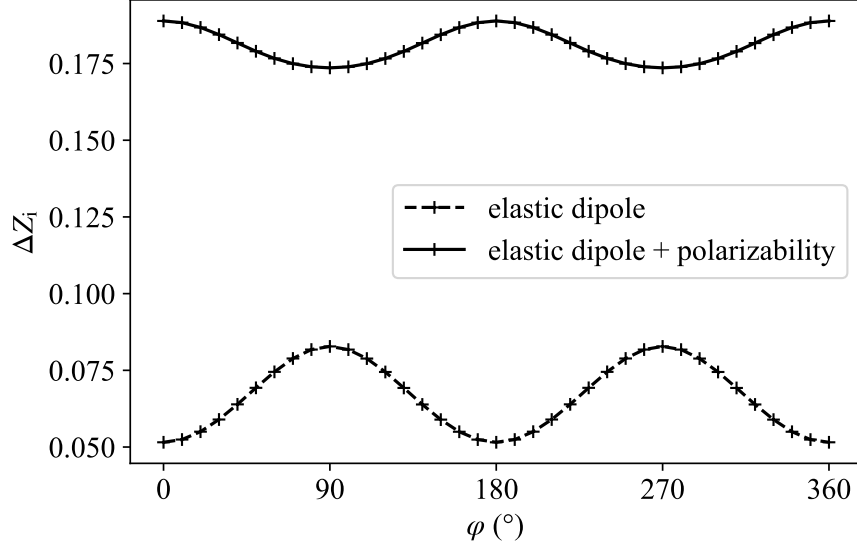


Figure 9: Difference of absorption efficiency of SIA  $\Delta Z_i$  as a function of  $\varphi$ , calculated with CDM for  $\theta = 90^\circ$ . The reference calculation which is subtracted corresponds to a hydrostatic stress with only  $P_{ij}$  taken into account. The dashed curve shows the evolution of  $\Delta Z_i$  if only  $P_{ij}$  is taken into account and the solid curve corresponds to the case where  $P_{ij}$  and  $\alpha_{ijkl}$  are considered.

606 Simulation results have been compared to analytical expressions of SIPA-  
607 AD and SIPA-I. For SIA, models are shown to be in reasonable agreement  
608 with simulations. Vacancies are very anisotropic in their saddle configuration,  
609 which induces strong lattice effects on the diffusion under stress. In this case  
610 the predictions of the models are not very accurate. The expression of Borodin  
611 and Ryazanov (B&R) for SIPA-AD includes lattice effects but it is assumed  
612 that defects are weakly anisotropic in their saddle configuration. It correctly  
613 predicts a maximum absorption rate of vacancies if the stress is applied along  
614 the  $\langle 100 \rangle$  direction with the largest projection on the dislocation line. However,  
615 the amplitude of SIPA-AD is underestimated by a factor 3. The expression  
616 for SIPA-I given by Woo (HSW model) relies on a simple isotropic description  
617 of defects and is unable to reproduce the angular dependence of absorption



618 efficiency, which is similar to that of SIPA-AD.

619 Our results show that dislocation climb velocity under irradiation is expected  
 620 to be the highest if the stress is approximately orthogonal to the dislocation  
 621 line, especially along the Burgers vector, and the lowest if the stress is applied  
 622 close to the  $\langle 100 \rangle$  direction with the largest projection on the dislocation line.  
 623 The dependence of these results on the symmetries of point defects in their  
 624 saddle configuration makes these conclusions likely transferable to other fcc  
 625 metals. The methodology used in this work can be applied to Frank dislocation  
 626 loops. It would be interesting to compare the obtained results to experimental  
 627 measurements of loop growth rates under stress [7], to better assess irradiation  
 628 creep mechanisms.

## 629 Appendix A. Modelling point defects as inhomogeneous inclusions

630 SIPA-I expressions (6)-(10) are more often given with notations related to  
 631 Eshelby inhomogenous inclusions. In this framework, a defect is considered as  
 632 a spherical inhomogeneity of bulk and shear moduli  $K^*$  and  $\mu^*$ , respectively,  
 633 with a misfit corresponding to the transformation strain  $e_{ij}^*$ . It is convenient to  
 634 consider an equivalent homogeneous inclusion of transformation strain  $e_{ij}^T$ , which  
 635 depends on  $e_{ij}^*$  and on the local external strain field (sum of the dislocation and  
 636 applied strain fields), as well as on the elastic moduli of the inclusion and of the  
 637 matrix [78]. The elastic dipole is related to the equivalent transformation strain  
 638 through [29]

$$P_{ij} = \Omega C_{ijkl} e_{kl}^T, \quad (\text{A.1})$$

639 with

$$C_{ijkl} = \left( K - \frac{2}{3}\mu \right) \delta_{ij}\delta_{kl} + \mu (\delta_{ik}\delta_{jl} + \delta_{il}\delta_{jk}). \quad (\text{A.2})$$

640 In SIPA-I models, the defect is considered as isotropic, so  $e_{kl}^T = \delta_{kl}e^T/3$ . We  
 641 obtain

$$P_{ij} = \Omega K e^T \delta_{ij} = P \delta_{ij}, \quad (\text{A.3})$$

642 where  $P$  is the quantity used in Eqs. (6)-(10). It is customary to use the strain  
 643 within the inclusion in the absence of external field,  $e_{ij}^0$ , related to  $e_{ij}^T$  by [78]

$$e_{ij}^0 = \mathcal{S}_{ijkl} e_{kl}^T, \quad (\text{A.4})$$

644 where  $\mathcal{S}_{ijkl}$  is the Eshelby tensor for a spherical inclusion:

$$\mathcal{S}_{ijkl} = \frac{5\nu - 1}{15(1 - \nu)} \delta_{ij} \delta_{kl} + \frac{4 - 5\nu}{15(1 - \nu)} (\delta_{ik} \delta_{jl} + \delta_{il} \delta_{jk}). \quad (\text{A.5})$$

645 The strain within the inclusion can be written as  $e_{kl}^0 = \delta_{kl} e^0/3$ , with

$$e^0 = \frac{1 + \nu}{3(1 - \nu)} e^T = \frac{1 + \nu}{3(1 - \nu)} \frac{P}{\Omega K}. \quad (\text{A.6})$$

646 We note that owing to Eqs. (17) and (A.3),  $e^T$  is the normalized relaxation  
 647 volume in a finite medium  $\Delta V^r/\Omega$ , whereas  $e^0$  is the normalized relaxation  
 648 volume in an infinite medium  $\Delta V^\infty/\Omega$ , the deformation being localized at the  
 649 position of the point defect [79].

650 By comparing the expressions of the interaction energy given by Eshelby [78]  
 651 and the one obtained from Eqs. (2) and (5), the following expressions are ob-  
 652 tained:

$$\alpha^K = -K\Omega \frac{3(1 - \nu)\Delta K}{3(1 - \nu)K + (1 + \nu)\Delta K} \quad (\text{A.7})$$

$$\alpha^\mu = -\mu\Omega \frac{15(1 - \nu)\Delta\mu}{15(1 - \nu)\mu + 2(4 - 5\nu)\Delta\mu}, \quad (\text{A.8})$$

653 with  $\Delta K = K^* - K$  and  $\Delta\mu = \mu^* - \mu$ .

## 654 **Appendix B. Set of deformation types to calculate polarizability ten-** 655 **sors**

656 The structure of the polarizability tensors of vacancies and SIAs in their  
 657 stable and saddle configurations depend on their symmetries. They are given in  
 658 Table B.2. To determine all coefficients, we consider several deformation types  
 659 (Tab. B.3). Since both initial ([100]) and final ([010]) configurations must be  
 660 relaxed under applied strain in order to calculate the saddle position, the results

Table B.2: Structure of polarizability tensors of vacancies and SIAs in their stable and saddle configurations.

	Stable configuration	Saddle configuration
	Cubic symmetry	Orthorhombic symmetry
Vacancy		For [100] to [010] jump
	$\begin{pmatrix} \alpha_{11} & \alpha_{12} & \alpha_{12} & 0 & 0 & 0 \\ \alpha_{12} & \alpha_{11} & \alpha_{12} & 0 & 0 & 0 \\ \alpha_{12} & \alpha_{12} & \alpha_{11} & 0 & 0 & 0 \\ 0 & 0 & 0 & \alpha_{44} & 0 & 0 \\ 0 & 0 & 0 & 0 & \alpha_{44} & 0 \\ 0 & 0 & 0 & 0 & 0 & \alpha_{44} \end{pmatrix}$	$\begin{pmatrix} \alpha_{11} & \alpha_{12} & \alpha_{13} & 0 & 0 & \alpha_{16} \\ \alpha_{12} & \alpha_{11} & \alpha_{13} & 0 & 0 & \alpha_{16} \\ \alpha_{13} & \alpha_{13} & \alpha_{33} & 0 & 0 & \alpha_{36} \\ 0 & 0 & 0 & \alpha_{44} & \alpha_{45} & 0 \\ 0 & 0 & 0 & \alpha_{45} & \alpha_{44} & 0 \\ \alpha_{16} & \alpha_{16} & \alpha_{36} & 0 & 0 & \alpha_{66} \end{pmatrix}$
	Tetragonal symmetry	Orthorhombic symmetry
SIA	For [100] configuration	For [100] to [010] jump
	$\begin{pmatrix} \alpha_{11} & \alpha_{12} & \alpha_{12} & 0 & 0 & 0 \\ \alpha_{12} & \alpha_{22} & \alpha_{23} & 0 & 0 & 0 \\ \alpha_{12} & \alpha_{23} & \alpha_{22} & 0 & 0 & 0 \\ 0 & 0 & 0 & \alpha_{44} & 0 & 0 \\ 0 & 0 & 0 & 0 & \alpha_{55} & 0 \\ 0 & 0 & 0 & 0 & 0 & \alpha_{55} \end{pmatrix}$	$\begin{pmatrix} \alpha_{11} & \alpha_{12} & \alpha_{13} & 0 & 0 & \alpha_{16} \\ \alpha_{12} & \alpha_{11} & \alpha_{13} & 0 & 0 & \alpha_{16} \\ \alpha_{13} & \alpha_{13} & \alpha_{33} & 0 & 0 & \alpha_{36} \\ 0 & 0 & 0 & \alpha_{44} & \alpha_{45} & 0 \\ 0 & 0 & 0 & \alpha_{45} & \alpha_{44} & 0 \\ \alpha_{16} & \alpha_{16} & \alpha_{36} & 0 & 0 & \alpha_{66} \end{pmatrix}$

Table B.3: Strain tensors and related variation in energies and dipole tensors due to polarizability. Tetragonal and orthorhombic symmetries refer to polarizability tensors given in Table B.2 ([100] orientation for the SIA and [100] to [010] jump respectively), unless specified.

strain matrix	cubic symmetry		tetragonal symmetry		orthorhombic symmetry	
	$-\frac{1}{2}\alpha_{ijkl}\varepsilon_j\varepsilon_k\varepsilon_l$	$-V\Delta\sigma_{ij} = \alpha_{ijkl}\varepsilon_k\varepsilon_l$	$-\frac{1}{2}\alpha_{ijkl}\varepsilon_j\varepsilon_k\varepsilon_l$	$-V\Delta\sigma_{ij} = \alpha_{ijkl}\varepsilon_k\varepsilon_l$	$-\frac{1}{2}\alpha_{ijkl}\varepsilon_j\varepsilon_k\varepsilon_l$	$-V\Delta\sigma_{ij} = \alpha_{ijkl}\varepsilon_k\varepsilon_l$
$\varepsilon_1 = \begin{pmatrix} \varepsilon & 0 & 0 \\ 0 & \varepsilon & 0 \\ 0 & 0 & \varepsilon \end{pmatrix}$	$-\frac{3}{2}(\alpha_{11} + 2\alpha_{12})\varepsilon^2$	$-V\Delta\sigma_{11} = (\alpha_{11} + 2\alpha_{12})\varepsilon$	$-\frac{1}{2}(\alpha_{11} + 2\alpha_{22} + 4\alpha_{12} + 2\alpha_{23})\varepsilon^2$	$-V\Delta\sigma_{11} = (\alpha_{11} + 2\alpha_{12})\varepsilon$ $-V\Delta\sigma_{22} = (\alpha_{12} + \alpha_{22} + \alpha_{23})\varepsilon$	$-\frac{1}{2}(2\alpha_{11} + 2\alpha_{12} + \alpha_{33} + 4\alpha_{13})\varepsilon^2$	$-V\Delta\sigma_{11} = (\alpha_{11} + \alpha_{12} + \alpha_{13})\varepsilon$ $-V\Delta\sigma_{33} = (2\alpha_{13} + \alpha_{33})\varepsilon$ $-V\Delta\sigma_{12} = (2\alpha_{16} + \alpha_{36})\varepsilon$
$\varepsilon_2 = \begin{pmatrix} \varepsilon & 0 & 0 \\ 0 & 0 & 0 \\ 0 & 0 & 0 \end{pmatrix}$	$-\frac{1}{2}\alpha_{11}\varepsilon^2$	$-V\Delta\sigma_{11} = \alpha_{11}\varepsilon$ $-V\Delta\sigma_{22} = \alpha_{12}\varepsilon$	$\frac{1}{2}\alpha_{11}\varepsilon^2$ $\frac{1}{2}\alpha_{22}\varepsilon^2$ $-\frac{1}{2}\alpha_{23}\varepsilon^2$ <sup>(a)</sup>	$-V\Delta\sigma_{11} = \alpha_{11}\varepsilon$ $-V\Delta\sigma_{22} = \alpha_{12}\varepsilon$ $-V\Delta\sigma_{11} = \alpha_{22}\varepsilon$ <sup>(a)</sup> $-V\Delta\sigma_{22} = \alpha_{12}\varepsilon$ <sup>(a)</sup> $-V\Delta\sigma_{33} = \alpha_{23}\varepsilon$ <sup>(a)</sup>	$-\frac{1}{2}\alpha_{11}\varepsilon^2$	$-V\Delta\sigma_{11} = \alpha_{11}\varepsilon$ $-V\Delta\sigma_{22} = \alpha_{12}\varepsilon$ $-V\Delta\sigma_{33} = \alpha_{13}\varepsilon$ $-V\Delta\sigma_{12} = \alpha_{16}\varepsilon$
$\varepsilon_3 = \begin{pmatrix} 0 & 0 & 0 \\ 0 & 0 & \varepsilon \\ 0 & \varepsilon & 0 \end{pmatrix}$	$-2\alpha_{44}\varepsilon^2$	$-V\Delta\sigma_{23} = 2\alpha_{44}\varepsilon$	$-2\alpha_{44}\varepsilon^2$ $-2\alpha_{35}\varepsilon^2$ <sup>(a)</sup>	$-V\Delta\sigma_{23} = 2\alpha_{44}\varepsilon$ $-V\Delta\sigma_{23} = 2\alpha_{55}\varepsilon$ <sup>(a)</sup>	$-2\alpha_{44}\varepsilon^2$	$-V\Delta\sigma_{23} = 2\alpha_{44}\varepsilon$ $-V\Delta\sigma_{13} = 2\alpha_{45}\varepsilon$
$\varepsilon_4 = \begin{pmatrix} 0 & \varepsilon & 0 \\ \varepsilon & 0 & 0 \\ 0 & 0 & 0 \end{pmatrix}$		Equivalent to $\varepsilon_3$	Equivalent to $\varepsilon_3$ on final configuration		$-2\alpha_{66}\varepsilon^2$	$-V\Delta\sigma_{11} = 2\alpha_{16}\varepsilon$ $-V\Delta\sigma_{33} = 2\alpha_{36}\varepsilon$ $-V\Delta\sigma_{12} = 2\alpha_{66}\varepsilon$

<sup>(a)</sup> On final configuration (SIA oriented along [010])

661 concerning the final configurations can also be exploited to obtain additional  
 662 data about coefficients of the polarizability tensor.

663 Figures B.10 and B.11 show the variation of energy due to polarizability,  
 664 called  $E^{(2)}$  (see Tab. B.3) extracted from DFT simulations (solid lines) and  
 665 calculated with the elastic model using polarizabilities deduced from residual  
 666 stress (in dashed lines). The variation of residual stress due to polarizabil-  
 667 ity,  $-V\Delta\sigma_{ij} = \alpha_{ijkl}\varepsilon_{kl}$ , is also shown. These two deformations (1 and 3, see  
 668 Tab. B.3) correspond to dilatation/compression and  $\langle 100 \rangle$  shear.

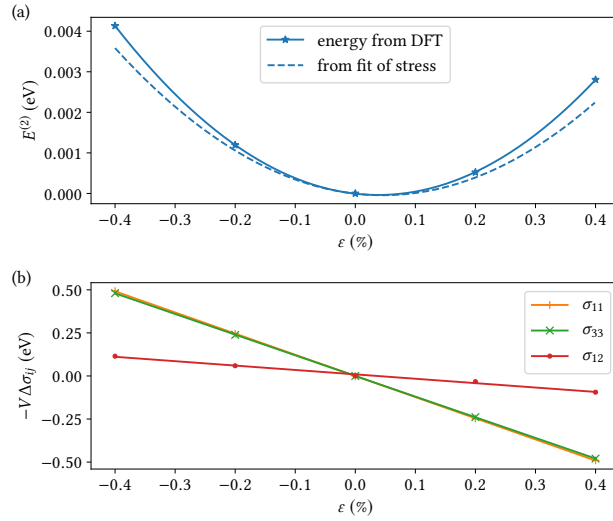


Figure B.10: Deformation 1 (dilatation/compression): (a) Variation of energy due to polarizability, extracted from DFT simulations (symbols with fit in solid lines) and calculated with the elastic model using polarizabilities extracted from residual stress (dashed lines). (b) Variation of residual stress (*i. e.* change in dipole tensors) due to polarizability, which is fitted with a linear function to extract polarizabilities.

## 669 Acknowledgments

670 T. J. acknowledges F. Willaime for discussions about DFT calculations and  
 671 Y. Le Bouar for discussions about polarizabilities. This work was performed  
 672 using HPC resources from GENCI-CINES (Grant 2020-A0100912414).

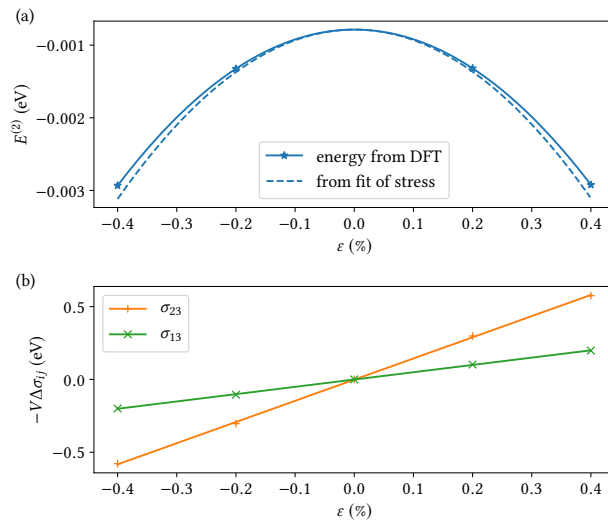


Figure B.11: Deformation 3 ((100) shear): (a) Variation of energy due to polarizability, extracted from DFT simulations (symbols with fit in solid lines) and calculated with the elastic model using polarizabilities extracted from residual stress (dashed lines). (b) Variation of residual stress (*i. e.* change in dipole tensors) due to polarizability, which is fitted with a linear function to extract polarizabilities.

673 **Data availability**

674 The relevant data are available within the article or from the authors upon  
675 reasonable request.

676 **References**

- 677 [1] J. R. Matthews, M. W. Finnis, Irradiation creep models – An overview, J.  
678 Nucl. Mater. 159 (1988) 257.
- 679 [2] F. Onimus, T. Jourdan, C. Xu, A. A. Campbell, M. Griffiths, 1.10 - irra-  
680 diation creep in materials, in: Comprehensive Nuclear Materials, Elsevier,  
681 2020, p. 310.
- 682 [3] P. R. Okamoto, S. D. Harkness, Stress-biased loop nucleation in irradiated  
683 type 316 stainless steels, J. Nucl. Mater. 48 (1973) 204.
- 684 [4] F. A. Garner, W. G. Wolfer, H. R. Brager, A reassessment of the role  
685 of stress in development of radiation-induced microstructure, in: J. A.  
686 Sprague, D. Kramer (Eds.), Effects of radiation on structural materials,  
687 ASTM STP 683, 1979, p. 160.
- 688 [5] D. Faulkner, R. J. McElroy, Irradiation creep and growth in zirconium  
689 during proton bombardment, in: J. A. Sprague, D. Kramer (Eds.), Effects  
690 of Radiation on Structural Materials: ASTM STP 683, 1979, p. 329.
- 691 [6] F. A. Garner, D. S. Gelles, Irradiation creep mechanisms: an experimental  
692 perspective, J. Nucl. Mater. 159 (1988) 286.
- 693 [7] S. Jitsukawa, Y. Katano, K. Shiraishi, F. A. Garner, The Behavior of  
694 Irradiation-Produced Dislocation Loops under External Stress during Elec-  
695 tron Irradiation, in: R. E. Stoller, A. S. Kumar, D. S. Gelles (Eds.), Effects  
696 of Radiation on Materials: 15th International Symposium, 1992, p. 1034.
- 697 [8] C. Xu, G. S. Was, Anisotropic dislocation loop distribution in alloy T91  
698 during irradiation creep, J. Nucl. Mater. 454 (2014) 255.

- 699 [9] W. G. Wolfer, Correlation of radiation creep theory with experimental ev-  
700 idence, *J. Nucl. Mater.* 90 (1980) 175.
- 701 [10] W. G. Wolfer, L. K. Mansur, J. A. Sprague, Theory of swelling and irradi-  
702 ation creep, in: M. L. Bleiberg, J. W. Bennett (Eds.), *Radiation Effects in*  
703 *Breeder Reactor Structural Materials*, 1977, p. 479.
- 704 [11] L. K. Mansur, Irradiation creep by climb-enabled glide of dislocations re-  
705 sulting from preferred absorption of point defects, *Philos. Mag. A* 39 (1979)  
706 497.
- 707 [12] C. H. Woo, E. J. Savino, Stress-induced preferred absorption due to saddle-  
708 point anisotropy: the case of an infinitesimal dislocation loop, *J. Nucl.*  
709 *Mater.* 116 (1983) 17.
- 710 [13] B. C. Skinner, C. H. Woo, Shape effect in the drift diffusion of point defects  
711 into straight dislocations, *Phys. Rev. B* 30 (1984) 3084.
- 712 [14] E. J. Savino, C. N. Tomé, Irradiation creep by stress-induced preferential  
713 attraction due to anisotropic diffusion (SIPA-AD), *J. Nucl. Mater.* 108 &  
714 109 (1982) 405.
- 715 [15] C. N. Tomé, H. A. Cecatto, E. J. Savino, Point-defect diffusion in a strained  
716 crystal, *Phys. Rev. B* 25 (1982) 7428.
- 717 [16] C. H. Woo, Irradiation creep due to elastodiffusion, *J. Nucl. Mater.* 120  
718 (1984) 55.
- 719 [17] V. A. Borodin, A. I. Ryazanov, The effect of diffusion anisotropy on dislo-  
720 cation bias and irradiation creep in cubic lattice materials, *J. Nucl. Mater.*  
721 210 (1994) 258.
- 722 [18] H. R. Schober, Single and multiple interstitials in FCC metals, *J. Phys. F:*  
723 *Metal Phys.* 7 (1977) 1127.
- 724 [19] E. J. Savino, Point defect-dislocation interaction in a crystal under tension,  
725 *Philos. Mag.* 36 (1977) 323.



- 726 [20] P. H. Dederichs, K. Schroeder, Anisotropic diffusion in stress fields, *Phys.*  
727 *Rev. B* 17 (1978) 2524.
- 728 [21] P. T. Heald, M. V. Speight, Steady-state irradiation creep, *Philos. Mag.* 29  
729 (1974) 1075.
- 730 [22] R. Bullough, J. R. Willis, The stress-induced point defect-dislocation in-  
731 teraction and its relevance to irradiation creep, *Philos. Mag.* 31 (1975) 855.
- 732 [23] P. T. Heald, M. V. Speight, Point defect behaviour in irradiated materials,  
733 *Acta Metall.* 23 (1975) 1389.
- 734 [24] W. Schilling, Self-interstitial atoms in metals, *J. Nucl. Mater.* 69 & 70  
735 (1978) 465.
- 736 [25] C. Varvenne, E. Clouet, Elastic dipoles of point defects from atomistic  
737 simulations, *Phys. Rev. B* 96 (2017) 224103.
- 738 [26] D. Carpentier, T. Jourdan, Y. Le Bouar, M.-C. Marinica, Effect of saddle  
739 point anisotropy of point defects on their absorption by dislocations and  
740 cavities, *Acta Mater.* 136 (2017) 323.
- 741 [27] T. Jourdan, A. Vattré, A continuous model including elastodiffusion for  
742 sink strength calculation of interfaces, *Comput. Mater. Sci.* 153 (2018) 473.
- 743 [28] R. Siems, Mechanical interactions of point defects, *Phys. Stat. Sol.* 30  
744 (1968) 645.
- 745 [29] E. Clouet, C. Varvenne, T. Jourdan, Elastic modeling of point-defects and  
746 their interactions, *Comp. Mater. Sci.* 147 (2018) 49.
- 747 [30] H. R. Schober, Polarizabilities of point defects in metals, *J. Nucl. Mater.*  
748 126 (1984) 220.
- 749 [31] A. D. Brailsford, R. Bullough, The rate theory of swelling due to void  
750 growth in irradiated metals, *J. Nucl. Mater.* 44 (1972) 121.

- 751 [32] A. D. Brailsford, R. Bullough, M. R. Hayns, Point defect sink strengths  
752 and void-swelling, *J. Nucl. Mater.* 60 (1976) 246–256.
- 753 [33] F. A. Nichols, On the estimation of sink-absorption terms in reaction-rate-  
754 theory analysis of radiation damage, *J. Nucl. Mater.* 75 (1978) 32.
- 755 [34] C. H. Woo, The sink strength of a dislocation loop in the effective medium  
756 approximation, *J. Nucl. Mater.* 98 (1981) 279.
- 757 [35] T. Jourdan, Influence of dislocation and dislocation loop biases on mi-  
758 crostructures simulated by rate equation cluster dynamics, *J. Nucl. Mater.*  
759 467 (2015) 286.
- 760 [36] A. A. Kohnert, L. Capolungo, Sink strength and dislocation bias of three-  
761 dimensional microstructures, *Phys. Rev. Mater.* 3 (2019) 053608.
- 762 [37] W. G. Wolfer, M. Ashkin, Diffusion of vacancies and interstitials to edge  
763 dislocations, *J. Appl. Phys.* 47 (1976) 791.
- 764 [38] C. H. Woo, Effects of an anisotropic dislocation structure on irradiation  
765 creep due to stress induced preferred absorption of point defects, *J. Nucl.*  
766 *Mater.* 80 (1979) 132.
- 767 [39] P. Ehrhart, P. Jung, H. Schultz, H. Ullmaier, Landolt–Börnstein, Numeri-  
768 cal Data and Functional Relationships in Science and Technology, Atomic  
769 Defects In Metals, Springer, 1991.
- 770 [40] I.-W. Chen, Anisotropic diffusion of point defects to edge dislocations, *J.*  
771 *Nucl. Mater.* 125 (1984) 52.
- 772 [41] G. F. Bouobda Moladje, L. Thuinet, C. Domain, C. S. Becquart, A. Legris,  
773 Phase-field calculations of sink strength in Al, Ni, and Fe: A detailed study  
774 of elastic effects, *Comput. Mater. Sci.* 183 (2020) 109905.
- 775 [42] V. A. Borodin, The effect of swelling on SIPA irradiation creep, *J. Nucl.*  
776 *Mater.* 225 (1995) 15.

- 777 [43] A. Vattré, T. Jourdan, H. Ding, M.-C. Marinica, M. J. Demkowicz, Non-  
778 random walk diffusion enhances the sink strength of semicoherent inter-  
779 faces, *Nat. Commun.* 7 (2016) 10424.
- 780 [44] E. Clouet, A. Bakaev, V. Borodin, Z. Chang, C. C. Fu, M. C. Marinica,  
781 P. Olsson, M. Posselt, D. Terentyev, P. Vladimirov, E. E. Zhurkin, Screen-  
782 ing of irradiation creep mechanisms using atomic-level simulation tools,  
783 Tech. rep., MATISSE project (2017).  
784 URL <http://fp7-matisse.eu/public-project-reports/>
- 785 [45] E. Clouet, S. Garruchet, H. Nguyen, M. Perez, C. S. Becquart, Dislocation  
786 interaction with C in  $\alpha$ -Fe: A comparison between atomic simulations and  
787 elastic theory, *Acta Mater.* 56 (2008) 3450.
- 788 [46] G. Kresse, J. Hafner, *Ab initio* molecular dynamics for liquid metals, *Phys.*  
789 *Rev. B* 47 (1993) 558.
- 790 [47] G. Kresse, J. Hafner, *Ab initio* molecular-dynamics simulation of the liquid-  
791 metal–amorphous-semiconductor transition in germanium, *Phys. Rev. B* 49  
792 (1994) 14251.
- 793 [48] G. Kresse, J. Furthmüller, Efficiency of ab-initio total energy calcula-  
794 tions for metals and semiconductors using a plane-wave basis set, *Comput.*  
795 *Mater. Sci.* 6 (1996) 15.
- 796 [49] G. Kresse, J. Furthmüller, Efficient iterative schemes for *ab initio* total-  
797 energy calculations using a plane-wave basis set, *Phys. Rev. B* 54 (1996)  
798 11169.
- 799 [50] P. E. Blöchl, Projector augmented-wave method, *Phys. Rev. B* 50 (1994)  
800 17953.
- 801 [51] G. Kresse, D. Joubert, From ultrasoft pseudopotentials to the projector  
802 augmented-wave method, *Phys. Rev. B* 59 (1999) 1758.

- 803 [52] N. Chetty, M. Weinert, T. S. Rahman, J. W. Davenport, Vacancies and  
804 impurities in aluminum and magnesium, *Phys. Rev. B* 52 (9) (1995) 6313.
- 805 [53] G. Henkelman, B. P. Uberuaga, H. Jónsson, A climbing image nudged  
806 elastic band method for finding saddle points and minimum energy paths,  
807 *J. Chem. Phys.* 113 (2000) 9901.
- 808 [54] M. A. Caro, S. Schulz, E. P. O'Reilly, Comparison of stress and total energy  
809 methods for calculation of elastic properties of semiconductors, *J. Phys.:*  
810 *Condens. Matter* 25 (2013) 025803.
- 811 [55] D. Connétable, P. Maugis, Effect of stress on vacancy formation and diffu-  
812 sion in fcc systems: Comparison between DFT calculations and elasticity  
813 theory, *Acta Mater.* 200 (2020) 869.
- 814 [56] V. Spirić, L. E. Rehn, K.-H. Robrock, W. Schilling, Anelastic relaxation  
815 due to single self-interstitial atoms in electron-irradiated Al, *Phys. Rev. B*  
816 15 (1977) 672.
- 817 [57] K.-H. Robrock, W. Schilling, Diaelastic modulus change of aluminum after  
818 low temperature electron irradiation, *J. Phys. F: Metal Phys.* 6 (3) (1976)  
819 303.
- 820 [58] P. H. Dederichs, C. Lehmann, A. Scholz, Change of elastic constants due  
821 to interstitials, *Z. Physik B* 20 (1975) 155.
- 822 [59] J. Holder, A. V. Granato, L. E. Rehn, Effects of self-interstitials and close  
823 pairs on the elastic constants of copper, *Phys. Rev. B* 10 (2) (1974) 363.
- 824 [60] L. E. Rehn, J. Holder, A. V. Granato, R. R. Coltman, F. W. Young, Jr,  
825 Effects of thermal-neutron irradiation on the elastic constants of copper,  
826 *Phys. Rev. B* 10 (2) (1974) 349.
- 827 [61] M. P. Puls, C. H. Woo, Diaelastic polarizabilities due to vacancies and  
828 interstitials in metals, *J. Nucl. Mater.* 139 (1986) 48.

- 829 [62] G. J. Ackland, Theoretical study of the effect of point defects on the elastic  
830 constants of copper, *J. Nucl. Mater.* 152 (1988) 53.
- 831 [63] H.-G. Haubold, Study of irradiation induced point defects by diffuse scat-  
832 tering, in: *Proc. Int. Conf. Fundamental Aspects of Radiation Damage in*  
833 *Metals*, 1975, p. 268.
- 834 [64] R. M. Emrick, P. B. McArdle, Effect of pressure on quenched-in electrical  
835 resistance in gold and aluminum, *Phys. Rev.* 188 (1969) 1156.
- 836 [65] P. Ehrhart, W. Schilling, Investigation of interstitials in electron-irradiated  
837 aluminum by diffuse-X-ray scattering experiments, *Phys. Rev. B* 8 (6)  
838 (1973) 2604.
- 839 [66] B. J. Buescher, R. M. Emrick, Pressure effect on defect migration in alu-  
840 minum, *Phys. Rev. B* 1 (10) (1970) 3922.
- 841 [67] R. C. Folweiler, F. R. Brotzen, The effect of quenched-in vacancies on the  
842 elastic modulus of aluminum, *Acta Metall.* 7 (1959) 716.
- 843 [68] H. R. Brager, F. A. Garner, E. R. Gilbert, J. E. Flinn, W. G. Wolfer,  
844 Stress-affected microstructural development and the creep-swelling interre-  
845 lationship, in: M. L. Bleiberg, J. W. Bennett (Eds.), *Radiation Effects in*  
846 *Breeder Reactor Structural Materials*, The Metallurgical Society of AIME,  
847 1977, p. 727.
- 848 [69] W. P. Kuykendall, W. Cai, Conditional convergence in two-dimensional  
849 dislocation dynamics, *Modelling Simul. Mater. Sci. Eng.* 21 (2013) 055003.
- 850 [70] D. T. Gillespie, A general method for numerically simulating the stochastic  
851 time evolution of coupled chemical reactions, *J. Comput. Phys.* 22 (1976)  
852 403.
- 853 [71] A. B. Bortz, M. H. Kalos, J. L. Lebowitz, A New Algorithm for Monte-  
854 Carlo Simulation of Ising Spin Systems, *J. Comput. Phys.* 17 (1975) 10.

- 855 [72] B. Zhang, C. Wheatley, P. Chen, X. Qian, M. J. Demkowicz, Shear strain  
856 alters the structure and migration of self-interstitial atoms in copper, *Phys.*  
857 *Rev. Mater.* 6 (2022) 053605.
- 858 [73] H. Flyvbjerg, H. G. Petersen, Error estimates on averages of correlated  
859 data, *J. Chem. Phys.* 91 (1989) 461.
- 860 [74] C. H. Woo, Intrinsic bias differential between vacancy loops and interstitial  
861 loops, *J. Nucl. Mater.* 107 (1982) 20.
- 862 [75] R. Bullough, M. R. Hayns, Irradiation-creep due to point defect absorption,  
863 *J. Nucl. Mater.* 57 (1975) 348.
- 864 [76] P. T. Heald, Radiation-induced creep and swelling, in: M. L. Bleiberg, J. W.  
865 Bennett (Eds.), *Radiation Effects in Breeder Reactor Structural Materials*,  
866 1977, p. 781.
- 867 [77] C. Xu, G. S. Was, Proton irradiation creep of FM steel T91, *J. Nucl. Mater.*  
868 459 (2015) 183.
- 869 [78] J. D. Eshelby, The determination of the elastic field of an ellipsoidal inclu-  
870 sion, and related problems, *Proceedings of the Royal Society of London.*  
871 *Series A. Mathematical and Physical Sciences* 241 (1957) 376.
- 872 [79] G. Leibfried, N. Breuer, *Point Defects in Metals I*, in: *Springer Tracts in*  
873 *Modern Physics*, Springer-Verlag, Berlin, 1978.